remote sensing

MDPI

Article

Effects of Solar Intrusion on the Calibration of the Metop-C Advanced Microwave Sounding Unit-A2 Channels

Banghua Yan [1,*], Changyong Cao [1] and Ninghai Sun [2]

[1] NOAA/STAR/Satellite Meteorology and Climatology, College Park, MD 20740, USA; changyong.cao@noaa.gov
[2] Global Science Technologies Inc., Greenbelt, MD 20770, USA; ninghai.sun@noaa.gov
* Correspondence: banghua.yan@noaa.gov; Tel.: +1-301-683-3602

Abstract: This study presents our first discovery about two abnormal problems in the blackbody calibration target associated with the antenna unit A2 in the Metop-C AMSU-A instrument. The problems include the anomalous patterns in both blackbody kinetic temperature (T_w) and radiative temperature (measured in warm count or C_w), and the time lag between orbital cycles of T_w and C_w. This study further determines solar intrusion as the root cause of the anomalous pattern problem. According to our analysis, solar illumination is constantly observed during each orbit near the satellite terminator, causing anomalous changes in C_w and T_w, characterized by sudden and abnormal increases typically for more than 16 min. The resultant maximum antenna temperature errors due to abnormal increases in C_w are approximately in the range from 0.15 K to 0.25 K, while the maximum errors due to the abnormal increase in T_w are in the range from 0.04 K to 0.07 K, varying with orbit, season, and channel. The time shift feature is characterized with a changeable time lag with the season in the T_w orbital cycle in comparison with the C_w cycle. The longest time lag up to about 18 min occurs in summer through early fall, while the time lag can be decreased down to about 9 min in winter through early spring. Hence, this study underscores the imperative need for future research to rectify radiance errors and reconstruct a more accurate long-term Metop-C AMSU-A radiance data set for channels 1 and 2, crucial for climate studies.

Keywords: microwave radiometry; Metop-A to Metop-C; NOAA-18 and NOAA-19; Advanced Microwave Sounding Unit-A (AMSU-A); solar intrusion; time lag; calibration accuracy; warm load calibration target; blackbody kinetic temperature; blackbody radiative temperature; channel 1 (23.8 GHz) and channel 2 (31.4 GHz); climate data record

Citation: Yan, B.; Cao, C.; Sun, N. Effects of Solar Intrusion on the Calibration of the Metop-C Advanced Microwave Sounding Unit-A2 Channels. *Remote Sens.* **2024**, *16*, 864. https://doi.org/10.3390/rs16050864

Academic Editor: Zhenzhan Wang

Received: 31 December 2023
Revised: 9 February 2024
Accepted: 20 February 2024
Published: 29 February 2024

1. Introduction

The Advanced Microwave Sounding Unit-A (AMSU-A) Instrument is a microwave radiometer consisting of 15 channels from 23.8 to 89 GHz, and its major specifications are shown in Table 1 [1–3]. Specifically, it has three antenna systems, A1-1, A1-2, and A2. The A1-1 system contains channels 6–7 and 9–15; A1-2 contains channels 3–5 and 8; A2 contains channels 1 and 2 [1–3]. The AMSU-A instrument is/was an operational payload onboard the National Oceanic and Atmospheric Administration (NOAA)-15 through NOAA-19 and Meteorological Operational satellite (Metop)-A through Metop-C. It is noted that the NOAA-16, NOAA-17, and Metop-A satellites were decommissioned on 9 June 2014, 10 April 2013, and 15 November 2021, respectively. The AMSU-A channel 15 onboard the Metop-B were disabled on 18 January 2017. In the past decades, intensive pre- and post-launch calibration/validation activities have been successfully applied to the AMSU-A instruments to derive high quality Earth scene antenna Temperature Data Record (TDR) and Sensor Data Record (SDR) data from Raw Data Record (RDR) (e.g., [4–14]). The AMSU-A data have contributed significantly to improvements in weather forecasts by Numerical Weather Prediction (NWP) Systems (e.g., [15–18]), retrievals of environmental

products [19–21], and monitoring of climate changes [22–24]. As the last unit in the series, the AMSU-A instrument onboard the Metop-C satellite not only ensures the continuation of those applications but also enables a longer AMSU-A data record.

Table 1. AMSU-A Instrument specifications [1–3].

Ch.	Center Frequency (MHz)	Conversion Bandwidth (MHz)	Temperature Sensitivity NEDT (K)
1	23,800	270	0.3
2	31,400	180	0.3
3	50,300	180	0.4
4	52,800	400	0.25
5	53,596 ± 115	170	0.25
6	54,400	400	0.25
7	54,940	400	0.25
8	55,500	330	0.25
9	fo = 57,290.344	330	0.25
10	fo ± 217	78	0.4
11	fo ± 322.2 ± 48	36	0.4
12	fo ± 322.2 ± 22	16	0.6
13	fo ± 322.2 ± 10	8	0.8
14	fo ± 322.2 ± 4.5	3	1.2
15	89,000	1500	0.5

In spite of wide applications of the AMSU-A TDR data, new improvements in the quality of AMSU-A data are valuable to further enrich the value of the data in various applications. Especially, the absolute radiometric calibration accuracy of the instrument data becomes more important for climate analysis due to its long data record. In addition, the calibration accuracy must be traceable to the National Institute of Standards and Technology (NIST) via secondary temperature standards. As a result, it is a continuous effort to monitor and detect new anomalies that may degrade the quality of the data. For example, the performance of AMSU-A TDR data quality in available channels are routinely monitored in the NOAA STAR Integrated Calibration and Validation System (ICVS) (https://www.star.nesdis.noaa.gov/icvs/index.php, accessed on 6 June 2012). A few key parameters about the quality of the AMSU-A TDR data are monitored in the ICVS website in a near-real-time mode, e.g., channel noise equivalent differential temperature (NEDT), gain, space view (cold) count, blackbody target (warm) count, kinetic or bulk temperature of the blackbody target, instrument shelf temperature, etc. In addition, the radiative transfer model simulation to the Earth scene brightness temperature is used to identify anomalous features in brightness temperatures at sounding channels.

In our monitoring process, it is first found that certain anomalous patterns always remain in the blackbody calibration target associated with kinetic temperature (T_w) and warm count (C_w) for AMSU-A channels 1 and 2 onboard Metop satellites. Those anomalous patterns are associated with sudden and unexpected increases for a few minutes during each orbit in both the kinetic temperature and the radiative temperature of the blackbody target (expressed as a warm count in the measurement) (see the analysis in Section 3 below). In addition, a time lag is observed in the orbital variation of the kinetic temperature in comparison with that of the radiative temperature (see the analysis in Section 3 below). According to our analysis, similar anomalous features also partially exist on the afternoon satellites NOAA-18 and NOAA-19 (the results are not shown in this study). To the authors' best knowledge, those discoveries are the first report for onboard AMSU-A instruments. The blackbody target anomalous problems were also not captured in the pre-launch analysis for all AMSU-A instruments. In practice, any error sources on the blackbody target can introduce uncertainties in the calibration and produce erroneous radiance or antenna temperatures because the blackbody target is used to determine Earth scene radiance or antenna temperatures [4,7,12]. Moreover, the window channels 1 and 2 for the AMSU-

A provide unique information to the other 12 temperature sounding channels from 3 through 14 by correcting for the surface emissivity, atmospheric liquid cloud water, and total precipitable water, thus playing a critical role in various applications of AMSU-A data. Therefore, it is desirable to analyze those anomalous features that happen in the blackbody calibration target in channels 1 and 2.

This study will present our first findings on detected anomalous features in the blackbody calibration target associated with T_w and C_w in channels 1 and 2 by using the Metop-C AMSU-A as a demonstration due to its significance in the AMSU-A data record. Moreover, solar intrusion will be determined as the root cause to the anomalous pattern problem based on a few established facts in this study. The solar intrusion in the AMSU-A instrument is investigated as the first report among pre-launch and post-launch calibration and validation activities. In this regard, however, the solar intrusion is not new to other satellite instruments. For instance, both instruments, Advanced Microwave Scanning Radiometer and WindSat, exhibited significant solar intrusion into the hot calibration load, leading to erroneous values for the hot load temperature [25–27]. Additionally, a solar intrusion effect was reported as early as 1998 for the Advanced Very High Resolution Radiometer (AVHRR) instrument flown on the NOAA polar orbiting satellites, causing an anomalous pattern in the blackbody warm count [28,29]. The AVHRR instrument suffered from solar contaminations when exposed to sunlight at spacecraft sunrise, related to a large scan angle within observations [28,29]. The AMSU-A instrument has similar large scan angles to the AVHRR, and the abnormal pattern problem in T_w and C_w does occur with large solar zenith angles. These facts motivate our identification of solar intrusion as the primary cause of the AMSU-A anomalous pattern issue observed in the AMSU-A. In addition to the anomalous pattern problem, this study will also examine the time lag phenomenon in the orbital variation of T_w in comparison with that of C_w, making the initial discovery. Its root cause is expected to be investigated in future studies after we have a good understanding of it.

This paper is organized as follows. The next section describes the calibration equation and operational processing for the AMSU-A TDR data. Section 3 investigates anomalous features in the blackbody calibration target for Metop-C AMSU-A in channels 1 and 2, while Section 4 addresses implications of the largest anomalous changes in both C_w and T_w for calibration accuracy of antenna temperatures. Section 5 investigates the root cause to the anomalous pattern problems in C_w and T_w. The final section summarizes and concludes our novel findings about the anomalous features and root cause. The discoveries of this study are anticipated to offer valuable insights into anomalous characteristics, affected regions, a root cause, and their impacts on radiance calibration accuracy. While this study focuses on Metop-C AMSU-A, the analysis method can be applicable for AMSU-A instruments on the NOAA-18, NOAA-19, Metop-A, and Metop-B, where solar intrusion is partially observed.

2. Calibration Equation and Operational Processing

In the AMSU-A calibration process [12], as given for other microwave radiometers such as the Advanced Technology Microwave Sounder (ATMS) [30], two calibration measurements, i.e., the cold space and the warm load, are used together with a non-linear radiometric calibration equation to determine Earth scene radiance R_s per scan, viewing angle, and channel, as shown below.

In the radiance domain [5,12,30,31],

$$R_s = R_c + (R_W - R_C)\frac{(C_s - C_c)}{(C_w - C_c)} + Q, \tag{1}$$

where

$$Q = \mu (R_W - R_C)^2 \frac{(C_S - C_w)(C_S - C_c)}{(C_w - C_c)^2}, \tag{2}$$

$$G = \frac{(C_w - C_c)}{(R_W - R_C)}. \tag{3}$$

Indices of the channel frequency and beam position (satellite scan viewing angle) are omitted in the variables of the equations throughout this study for brevity. In the above equations, R_S represents the Earth scene radiance of individual channels; C_S is the radiometric count from the Earth scene target; G is the channel calibration gain; C_w and C_c denote the blackbody and space count, respectively. In addition, R_W and R_C denote the radiance corresponding to T_W and T_c, respectively, where T_W denotes the platinum resistance thermometer (PRT) temperature of the warm load converted from measured radiometric counts, and its calculation and calibration are given in [5]. The conversion coefficients from counts to PRT temperatures such as T_W are included in TDR data. T_c is cosmic temperature after certain correction [12], and Q is the nonlinearity of instrument square-law detector that is a function of nonlinearity parameter μ. Variables, i.e., R_C, R_W, and R_S, in the above equations are performed in radiance with the unit of mW/(m^2·sr·cm^{-1}). Table 2 provides a summary about physical explanations of major variables in the equations in this study.

Table 2. Variables in the equations and explanations.

Symbol	Quantity
R_S	Earth scene radiance, $\frac{mW}{m^2 \cdot sr \cdot cm^{-1}}$
T_A	Antenna temperature in Kelvin, which is converted from R_S by using the inverse of Planck function
T_W	Kinetic or bulk temperature of the blackbody target (warm load), also named as warm load PRT temperature
T_c	Cosmic temperature after certain corrections [12]
R_W	Radiance corresponding to T_W using Planck function
R_C	Radiance corresponding to T_c using Planck function
C_w	Warm load radiometric count (warm count), corresponding to the radiative temperature of the blackbody target
C_c	Cold space radiometric count (cold count)
C_S	Earth scene radiometric count (scene count)
Q	Nonlinearity of instrument square-law detector in radiance domain
Q_T	Nonlinearity in temperature domain
μ	Nonlinearity parameter μ in radiance domain
μ_T	Nonlinearity parameter μ in temperature domain
G	Calibration channel gain in the domain of radiance
G_T	Calibration channel gain in the domain of temperature

The calibration equation in the radiance domain can be converted to the antenna temperature T_A domain. T_A has the same format as that in (1) to (3) except for a conversion of each parameter from radiance to brightness temperature by using the Planck function instead of Rayleigh–Jeans approximation [32]. The nonlinearity Q in (2) needs to be replaced by a new variable Q_T that is computed using the same expression as Q in (2) except in the temperature domain.

In the operational processing of AMSU-A data in channels 1 and 2, hereinafter named as AMSU-A2 channels since they are associated with the antenna unit A2, six PRT sensors are distributed at the base of the in-flight warm calibration target to determine its kinetic or bulk temperature, T_w, which is often referred to as PRT temperature due to the use of the PRT sensors [31,33]. It is actually the average of six PRT sensors for the AMSU-A2 channels unless new descriptions are given. According to our analysis, the uncertainty of T_w per PRT sensor is in an order of 0.05 K. This estimate is referred to the ICVS web-based monitoring tool: https://www.star.nesdis.noaa.gov/icvs/status_MetOPC_AMSUA.php, accessed on 5 April 2019. Based on the measurement error analysis with small sampling size, the uncertainty of the averaged trends after satellite merging is expressed as $\pm\frac{\Delta}{2\sqrt{K}}$ [34,35]. In this study, Δ ($\approx$0.05 K/PRT sensor) denotes the maximum relative error for one PRT sensor from another PRT sensor used in the AMSU-A2 unit, and K (=6) the number of PRT sensors used for the AMSU-A2 unit. As a result, the averaged uncertainty of the T_w is about 0.01 K.

The warm count C_w in (1) is a weighted average by using originally measured C_W data within seven neighboring scans to reduce fluctuations of the original C_W along the scan due to instrument noise [5,33]. For each scan, the weighted-average warm (cold) count, i.e., $\overline{C}_x$, is obtained by convolving C_x (where $x = w$ or c) over $(2N + 1)$ neighboring scan lines using certain weighting values, as shown below.

$$\overline{C}_x(t_j) = \frac{\sum_{i=-N}^{N} W_i C_x(t_i)}{\sum_{i=-N}^{N} W_i}. \quad (4)$$

Here, t_j denotes the time of the current scan line; t_i represents the time of the scan lines just before or after the current scan line; N is the number of scans used in the weighing process before or after the current scan line; w_i represents a set of triangular weights relative to the calculated scan at t_j. For example, when $N = 3$, there are a total of seven scan lines in (4), w_i takes the values of 1, 2, 3, 4, 3, 2, and 1 for the seven scan lines with $i = 1, 2, 3, 4, 3, 2,$ and 1, respectively. In the operational processing, $C_x(t_i)$ in (4) is the average of two measurements, namely $C_x^{1st}(t_i)$ and $C_x^{2nd}(t_i)$, from different viewing points per scan, i.e., $C_x(t_i) = \left[C_x^{1st}(t_i) + C_x^{2nd}(t_i)\right]/2$.

The calibration equation in (1) assumes that there are no extraneous radiations other than radiation from the calibration target. This assumption works well for pre-launch or post-launch AMSU-A instruments for most of the AMSU-A channels. As an example, Figure 1 shows time series of two kinetic temperatures that are associated with the antenna unit A1-1 and A1-2, and the warm counts at the two channels corresponding to the A1-1 and A1-2, by using approximately two orbits of operational AMSU-A TDR data on 28 May 2021. Both T_W and $\overline{C}_{w7}$ exhibit an expected orbital cycle from orbital minimum (peak) to an orbital peak (minimum) due to changes in the instrument temperature during ascending and descending observations. Here, $\overline{C}_{w7}$ represents the weighting average of seven neighboring scan lines using (4). Additionally, the variations of T_W and $\overline{C}_{w7}$ generally align with the averaged trend of the data, either decreasing from p_{max} to p_{min} or increasing from p_{min} to p_{max}, as depicted by the conceptual linear fitting lines in the figure. As anticipated, certain fluctuations persist within orbital variations due to instrument noise, causing a few outliers that exceed largely the normal trend at random positions. For example, despite the application of the seven-neighboring average in (4), $\overline{C}_{w7}$ still frequently exhibits large fluctuations during orbital observations. The fluctuations do not follow a stable pattern, and they do not occur at a consistent position from one orbit to another orbit. In addition, T_W typically displays a small fluctuation within ± 0.01 K for a couple of minutes before it jumps or drops to a higher or lower level of the value, which is consistent with the calculation of the averaged T_w uncertainty by using $\pm\frac{\Delta}{2\sqrt{K}}$. Overall, the observed features are expected, without anomalous patterns.

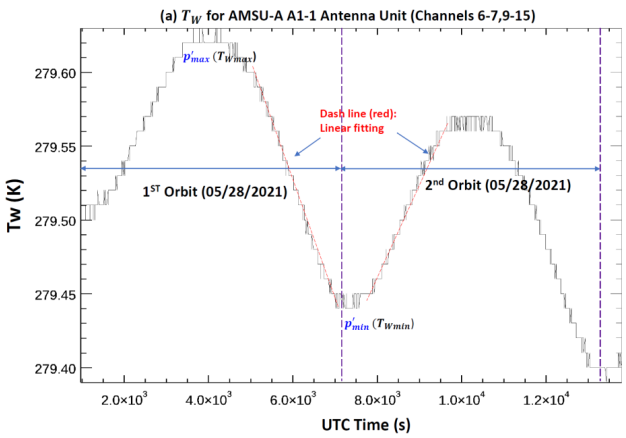

Figure 1. *Cont.*

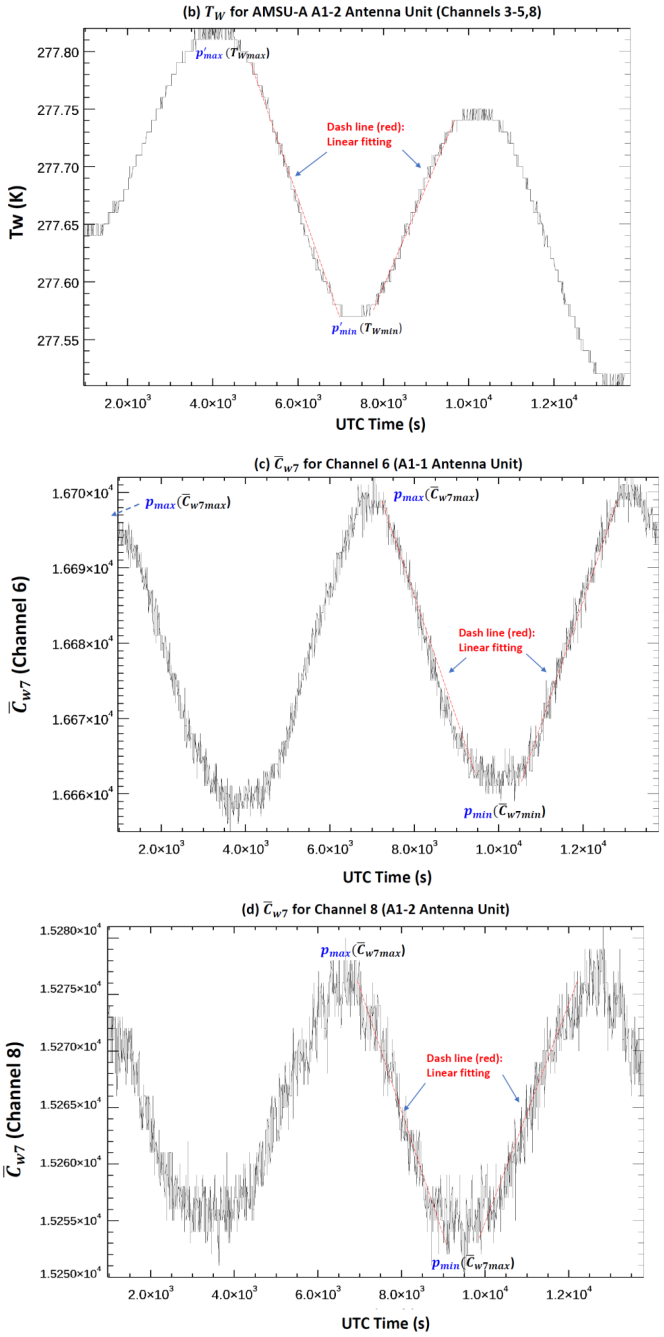

Figure 1. Time series of the blackbody target kinetic temperature (T_w) associated with antenna unit A1-1 and A1-2 and the radiometric count ($\overline{C}_{w7}$) for one selected channel associated with the A1-1 and A1-2, respectively, by using two orbits of the Metop-C AMSU-A TDR data on 28 May 2021. Here, $\overline{C}_{w7}$ represents the weighting average of seven neighboring scan lines using (4). (**a**) T_w associated with the antenna unit A1-1. (**b**) T_w associated with the antenna unit A1-2. (**c**) $\overline{C}_{w7}$ in channel 6 associated with the antenna unit A1-1. (**d**) $\overline{C}_{w7}$ in channel 8 associated with the antenna unit A1-2. In the figure, the pairs (p'_{min} and p'_{max}) and (p_{min} and p_{max}) represent the minimum and maximum area in T_w and $\overline{C}_{w7}$, corresponding to (T_{Wmin} and T_{Wmax}) and ($\overline{C}_{w7min}$ and$\overline{C}_{w7max}$). Due to the fluctuations in the data, they do not signify accurate positions in the figure. The dash lines in red are also a conceptual demonstration for the average trend of the data along a decreased or increased direction.

3. Anomalous Features in AMSU-A2 Blackbody Calibration Target

In reality, the relationship between the calibration targets and the required radiance in (1) could be disrupted if one of the following problematic situations occurs: one situation

is that the radiometer receives an extraneous radiation, such as a solar intrusion from sources other than the blackbody, during the blackbody view; another situation is that a discrepancy exists in either phase (time) or magnitude between the orbital variations of T_W and C_w. Unfortunately, both problems occur for the AMSU-A instrument associated with channels 1 and 2, as described below.

3.1. Anomalous Features

Figure 2a,b show the time series of T_W and $\overline{C}_{w7}$ for the operational data during 14 orbits on 28 May 2021 for Metop-C AMSU-A channels 1 and 2, respectively. An abnormal pattern with sudden jumps persistently remains in each orbit of T_W and $\overline{C}_{w7}$ in comparison with an averaged normal variation trend in the absence of the abnormal pattern problem. A thorough discussion will be provided alongside a detailed time series zoom-in depicted in Figure 3 below. The affected area locates at a similar position during each orbit in a day for the two channels. In addition, the orbital variation of T_W delays for certain time in comparison with that of C_W.

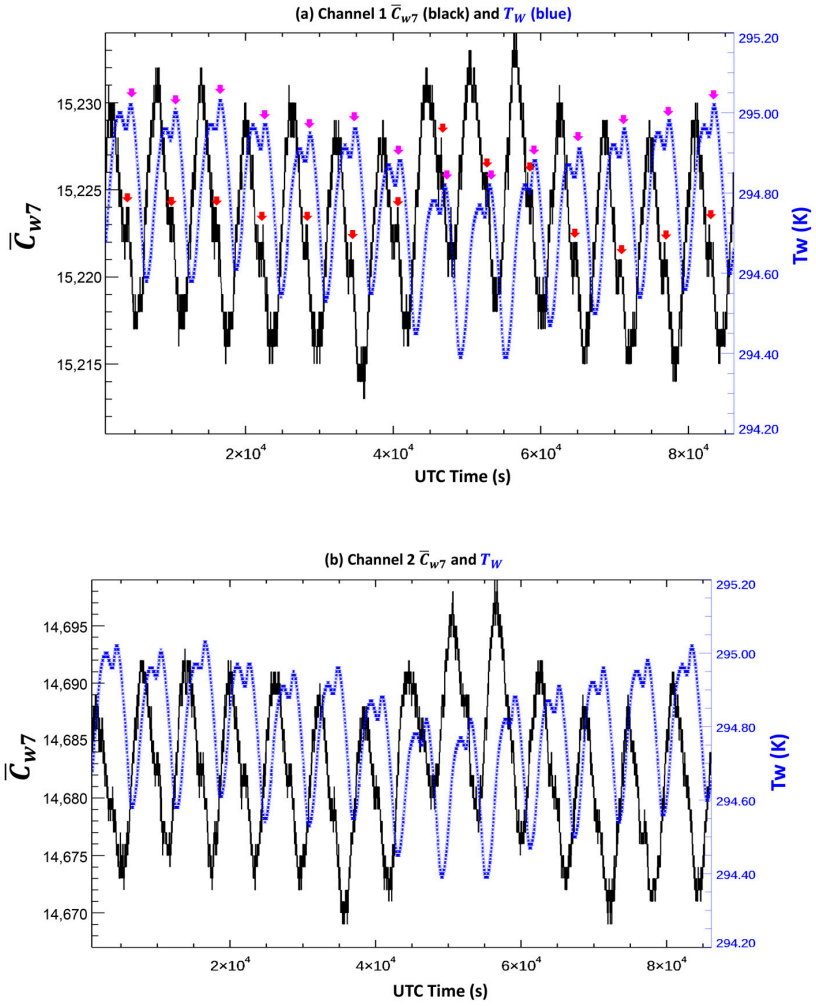

Figure 2. Time series of the Metop-C AMSU-A2 blackbody target radiometric count ($\overline{C}_{w7}$) and kinetic temperature (T_w) for channels 1 and 2 by using two orbits of observations on 28 May 2021. T_W is hereinafter the kinetic temperature of the blackbody associated with the AMSU-A antenna unit A2 unless other descriptions are given. (**a**) Channel 1. (**b**) Channel 2. The red and pink arrows in (**a**) indicate approximate positions of the anomaly peak for $\overline{C}_{w7}$ and T_w, respectively, for each orbit in channel 1. Those positions are applicable for (**b**).

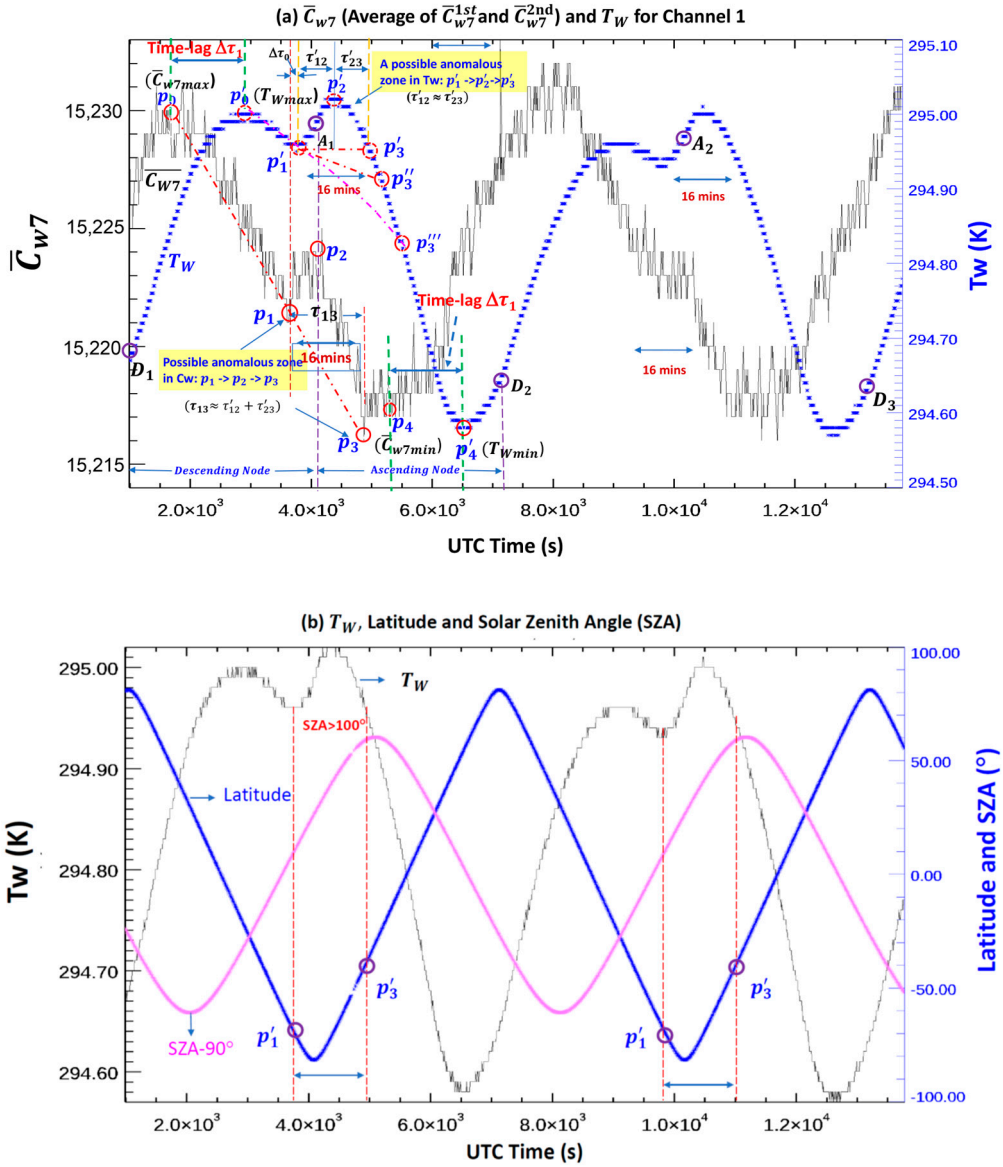

Figure 3. Time series of Metop-C AMSU-A2 blackbody target radiometric count ($\overline{C}_{w7}$), kinetic temperature (T_w), latitude, and SZA within approximately two orbits of observations, where the data were collected on 28 May 2021. (**a**) $\overline{C}_{w7}$ and T_w for channel 1. (**b**) Latitude, SZA, and T_w. In (**a**), for a conceptual demonstration, three positions in $\overline{C}_{w7}$, i.e., p_1, p_2, and p_3, and three positions in T_w, i.e., p_1', p_2', and p_3' are marked, approximately representing the starting, maximum, and ending positions in the presence of solar intrusion for $\overline{C}_{w7}$ and T_w, respectively. Two points, p_3'' and p_3''', are two possible positions when the anomaly should stop. The points A_1 and A_2 denote approximately the initial locations of the ascending nodes in the two orbits. Similarly, D_1~D_3 designate the starting positions of the descending node during each orbit. $\overline{C}_{w7max}$ and $\overline{C}_{w7min}$ (T_{wmax} and T_{wmin}) represent the areas where $\overline{C}_{w7}$ (T_w) reaches its maximum and minimum in the first orbit, respectively. In (**b**), the starting and ending positions with the anomalous pattern in T_w during the two orbits are marked with p_1' and p_3'.

To better understand these anomalous features, Figure 3a focuses on two orbits of the data in channel 1 that were used in Figure 2. In addition, the latitude and solar zenith angle (SZA) are added as Figure 3b. Several specific positions in the time series of the data, e.g., starting, peak, and ending positions of the anomalous pattern regions in both $\overline{C}_{w7}$ and T_w, are marked in the first orbit to highlight the regions in the presence of the anomalies. Two important features are observed based on the figure, as described below.

Firstly, both $\overline{C}_{w7}$ or T_W exhibit abnormal patterns with unexpected sudden increases in comparison with an averaged normal variation trend for more than 16 min during each orbit of the observations, which are entirely different the instrument noise-caused fluctuations in Figure 1 above. A detailed explanation about this is provided below.

For a conceptual demonstration, two pairs of points (p_1 and p_3) and (p'_1 and p'_3) in Figure 3a indicate the approximate starting and ending positions of noticeable abnormal patterns during the first orbit for $\overline{C}_{w7}$ and T_w, respectively. The resultant variations in both $\overline{C}_{w7}$ and T_W during the marked areas significantly deviate from the averaged trend of the data in the absence of the anomalies. Recall that in the absence of the anomaly, T_w associated with antenna unit A1-1 and A1-2 can exhibit an orbital cycle with a relatively smooth trend from a minimum (or maximum) to a maximum (or minimum) (see Figure 1a,b above), where there was no abnormal problem. Therefore, for a conceptual demonstration, a linear dot-dash line in red is added in Figure 3a, from p_0 ($\overline{C}_{w7max}$) to p_3, approximately representing the averaged normal trend of $\overline{C}_{w7}$ in the absence of the anomaly along the decreasing direction during the first orbit of the observations. Similarly, a pink nonlinear dot-dash curve from p'_1 to p'_4 roughly represents the averaged normal trend of T_W in the decreasing direction. Other methods can also be used to fit the normal trend of the data, all indicating the occurrence of the abnormal pattern. More importantly, these abnormal patterns are wholly distinct from the aforementioned noise-caused fluctuations: the anomaly pattern lasts for an extended period (more than 16 min, as seen on the scale in the figure) and constantly persists over similar locations during each of 14 orbits in a day (see Figure 2 above). Additionally, as shown in Figure 3b, the SZAs associated with the abnormal patterns are over 100°, indicating a possible impact of solar intrusion on the AMSU-A blackbody target associated with the antenna unit A2 (see the analysis in Section 5 for details). These conclusions are also applicable for channel 2.

As analyzed above, the abnormal patterns in both $\overline{C}_{w7}$ and T_w have been observed in comparison with corresponding averaged-normal variation trend in the absence of the degraded data. However, accurately determining the starting and ending positions is challenging due to remaining fluctuations in the data. This study does not attempt to develop a physical model due to lack of sufficient information. Instead, we present an empirical method to estimate the starting and ending positions of the anomaly to capture main abnormal features. T_W exhibits better stability over time (scan) than $\overline{C}_{w7}$, where the fluctuation in T_W usually is less than 0.01 K. Consequently, we will primarily use the anomalous features of T_W to estimate the starting and ending positions, while those of $\overline{C}_{w7}$ will be used to confirm the analysis conclusion.

Using the first orbit of the data as a demonstration, p'_1 in Figure 3a is used to represent the starting time of the T_W anomaly pattern. It is defined as the local minimum position between p'_0 (a peak of T_w in the first orbit of observations in the absence of the abnormal occurrence) and p'_2 (a local maximum due to the anomaly occurrence). In the absence of the anomaly, T_w associated with antenna unit A2 should exhibit an orbital cycle with a relatively smooth trend from a minimum (or maximum) to a maximum (or minimum), similar to that in the antenna units A1-1 and A1-2 [see Figure 1a,b above], where there was no abnormal problem. It is interesting to note that the position p'_1 is in proximity to the satellite terminator about 8 min prior to the spacecraft sunset (see Section 5 for details), with approximately one minute of uncertainty. p'_1 is also only about a couple of minutes (see $\Delta\tau_0$ in Figure 3a) after the local minimum position of $\overline{C}_{w7}$ (see p_1 in the figure) when the $\overline{C}_{w7}$ anomaly problem starts. Those two facts further confirm the reasonability of the estimated starting position for the T_W anomaly pattern. Regarding the time-shift of about 2 min between the positions of p_1 and p'_1, marked with $\Delta\tau_0$ in the figure, it approximately denotes the time lag of the T_w anomaly behind the $\overline{C}_{w7}$ anomaly. This time lag is thought to be related to the overall time lag in the orbital cycle of T_W and that of $\overline{C}_{w7}$, which will be addressed soon.

For the ending position of the anomalous pattern, we only make a conservative estimate in the following analysis. According to our analysis in Section 4 below, an

additional radiation resulting from solar intrusion is responsible for the occurrence of the anomaly pattern. The resulting T_W anomaly in the blackbody kinetic temperature should experience the following variations: in the first half-cycle, the T_W anomaly should gradually increase from zero (the solar intrusion just starts) to a peak (the solar intrusion just ends); in the second half-cycle, the T_W anomaly should gradually decrease from the peak to zero due to a cooling process. In this study, this cycle is approximately assumed to be symmetric. With this approximation, the time length of two half-cycles is the same.

Using the first orbit of the data in Figure 3a as an example, the resultant anomalous increase in T_W varies from a minimum (~zero) at p'_1 to a peak (~0.07 K) at p'_2, corresponding to the starting and stopping time of the solar intrusion, with a time length τ'_{12}. Subsequently, the anomalous variation of T_W gradually decreases from the peak at p'_2 to zero anomaly at p'_3, corresponding to a time τ'_{23}. With the above symmetric approximation, $\tau'_{12} \approx \tau'_{23}$. Hence, p'_3 can be estimated using this approximation, representing the ending position of the T_W anomaly pattern. However, it should be emphasized that the symmetric assumption mostly underestimates the time length of the T_W anomalous pattern. In view of Figure 3a, the variational pattern of T_w after p'_3 is still not smooth for at least a few minutes. This implies that these T_w values might still be affected by the solar intrusion effect, although the anomaly is weak. As a result, the impact of the anomaly would be increased if the accurate ending position of the anomaly is a position after p'_3 such as p''_3 or p'''_3. Therefore, the current method only provides a very conservative estimate about the anomaly length and magnitude.

With the estimated T_W anomaly length, furthermore, we can derive the approximate ending position of the $\overline{C}_{w7}$ anomaly with an additional approximation: the time length of the $\overline{C}_{w7}$ anomaly is supposed to be the same as that of the T_w anomaly. For Figure 3a, the p_3 is defined as the ending position of the $\overline{C}_{w7}$ anomaly pattern, where the time length (τ_{13}) from p_1 to p_3 equals to that of the T_W anomaly pattern ($\tau'_{12} + \tau'_{23}$), i.e., $\tau_{13} \approx \tau'_{12} + \tau'_{23}$. It is interesting to notice that p_3 is also nearby a local minimum point in $\overline{C}_{w7}$ before $\overline{C}_{w7}$ returns to a normal pattern. Therefore, this coincidence of the results using two different methods indicates the basic reasonability of the approximations.

Secondly, after gaining a good understanding of the anomalous patterns, we can analyze another important abnormal feature from Figure 3a: a time lag persists constantly throughout the entire time series of T_W and $\overline{C}_{w7}$ during the first two orbits. This feature actually exists in each of the orbits in Figure 2 above. This time lag indicates the blackbody kinetic (bulk) temperature, T_W, always responds more slowly than the blackbody radiative temperature measured in warm count.

Currently, we are unable to calculate accurately the lag length using the features in the figure due to fluctuations in both T_W and $\overline{C}_{w7}$, although the time lag feature is visually observed in the figure. Instead, we only make an approximate estimation by computing the time difference between the peaking or minimum positions in the orbital $\overline{C}_{w7}$ and T_W in the absence of the anomaly patterns.

For instance, two points, p_0 and p'_0, are added in Figure 3a to symbolize the positions where $\overline{C}_{w7}$ and T_w reach to the maximum without the anomaly pattern, respectively. Certainly, the instrument noise causes instability of the maximum position, especially for $\overline{C}_{w7}$. For T_w, the values around p'_0 can be nearly constant for a few hundreds of seconds. Hence, p'_0 is defined as the middle point within this nearly constant peaking range, representing the maximum position in T_w during the first orbit of the observations without considering the anomaly-caused peaking position.

A similar calculation is made for $\overline{C}_{w7}$ to locate p_0, which denotes the middle position in the peaking area to reduce the impact of fluctuations. As a result, the time difference between p_0 and p'_0 is about 18 min, marked as $\Delta\tau_1$ in Figure 3a. This estimation is further confirmed by using the time difference between p_4 and p'_4, which correspond to the averaged (middle point) minimum positions in $\overline{C}_{w7}$ and T_w in the first orbit. Additionally, the time lag between the two anomalous patterns, seen as $\Delta\tau_0$ in the figure, should be related to this overall time lag. However, this time lag (a couple of minutes) is much shorter than

the overall time lag between the orbital variations of $\overline{C}_{w7}$ and T_w. Similar features exist for channel 2 and other orbits. However, it is still not clear what causes the differences in the time lags between the orbital cycles and the anomalies in $\overline{C}_{w7}$ and T_w, which defers to further study.

3.2. More Discussions

The above analysis has addressed two important problematic features that occurred in $\overline{C}_{w7}$ and T_w by using one day of the Metop-C AMSU-A data in channels 1 and 2. A further discussion is still necessary to better characterize the anomalous problems. For instance, do warm counts in individual measurements, i.e., $C_x^{1st}(t_i)$ and $C_x^{2nd}(t_i)$, have similar abnormal features? Is the abnormal problem caused by the instrument noise (fluctuations)? Is it possible to use a polynomial function to fit abnormal patterns in $\overline{C}_{w7}$ and T_w to facilitate a more objective analysis of the issues in future studies? Do the observed abnormal features constantly persist during each of the orbits? Below are discussions for those questions.

Firstly, $\overline{C}_{w7}$ in the above figures represents an average of measurements at two different viewing directions. To identify any irregular characteristics in individual measurements, we also utilize (4) for two separate measurements (namely, $C_x^{1st}(t_i)$ and $C_x^{2nd}(t_i)$) to compute the average across seven scans of the data, i.e., $\overline{C}_x^{1st}(t_j)$ and $\overline{C}_x^{2nd}(t_j)$. Furthermore, we conduct an analysis of time series data for both $\overline{C}_{w7}^{1st}$ and $\overline{C}_{w7}^{2nd}$ using (2) for each of the individual measurements. Both $\overline{C}_{w7}^{1st}$ and $\overline{C}_{w7}^{2nd}$ exhibit anomalous characteristics similar to $\overline{C}_{w7}$ (the figure is omitted). This suggests that the warm counts at two different viewing directions also perform anomalously. Hereinafter, we will utilize the averaged of these two individual measurements in accordance with our operational processing.

Secondly, it is necessary to understand whether the anomalous patterns and time lag are caused by the instrument noise-caused fluctuations. The noise-caused fluctuations in the time series of $\overline{C}_{w7}$ and T_w can be largely smoothed through averaging more neighboring scans. Hence, a sensitivity analysis is conducted by applying an average to more neighboring scans of the data on 28 May 2021. The sensitivity analysis consists of seven types of averaged data: N = 3, 4, 5, 6, 7, 10, and 20, in (4), which correspond to 7, 9, 11, 13, 15, 21, and 41 neighboring scans, respectively. As a result of this design, seven distinct sets of averaged data are obtained for the warm count and kinetic temperature: $\overline{C}_{w7}$, $\overline{C}_{w9}$, $\overline{C}_{w11}$, $\overline{C}_{w13}$, $\overline{C}_{w15}$, $\overline{C}_{w21}$, $\overline{C}_{w41}$ and $\overline{T}_{w7}$, $\overline{T}_{w9}$, $\overline{T}_{w11}$, $\overline{T}_{w13}$, $\overline{T}_{w15}$, $\overline{T}_{w21}$, $\overline{T}_{w41}$. Both $\overline{C}_{w7}$ and $\overline{T}_{w7}$ are included for comparison since they represent data from the same orbit length.

As a demonstration, Figure 4a,b show the time series of warm count and kinetic temperature during the first orbit period through averaging 11 and 21 neighboring scans, i.e., $\overline{C}_{w11}$, $\overline{C}_{w21}$, and $\overline{T}_{w11}$, $\overline{T}_{w21}$. The noise-caused fluctuations in warm count are smoothed with slightly reduced values of both maximum and minimum during an orbit of observations through averaging more neighboring scans. However, the anomalous features of the pattern are not changed in warm count and kinetic temperature. A similar time lag with about 18 min is also observed in the kinetic temperature orbital cycle behind the warm count cycle, based on the results by using more neighboring scans. Regarding the time lag between the anomalies, the kinetic temperature anomaly occurs for about 2 min behind the warm count anomaly by using 11 and 21 neighboring scans, which is also similar to that by using 7 neighboring scans in the average. In general, the abnormal pattern problem persists in the blackbody calibration target across all types of averaged data sets. The time lag magnitudes also show consistency across different averaging methods. Thus, these findings suggest that the observed abnormal features are not a result of fluctuations. Increasing the number of neighboring scans averaged can indeed enhance the identification of these abnormal issues.

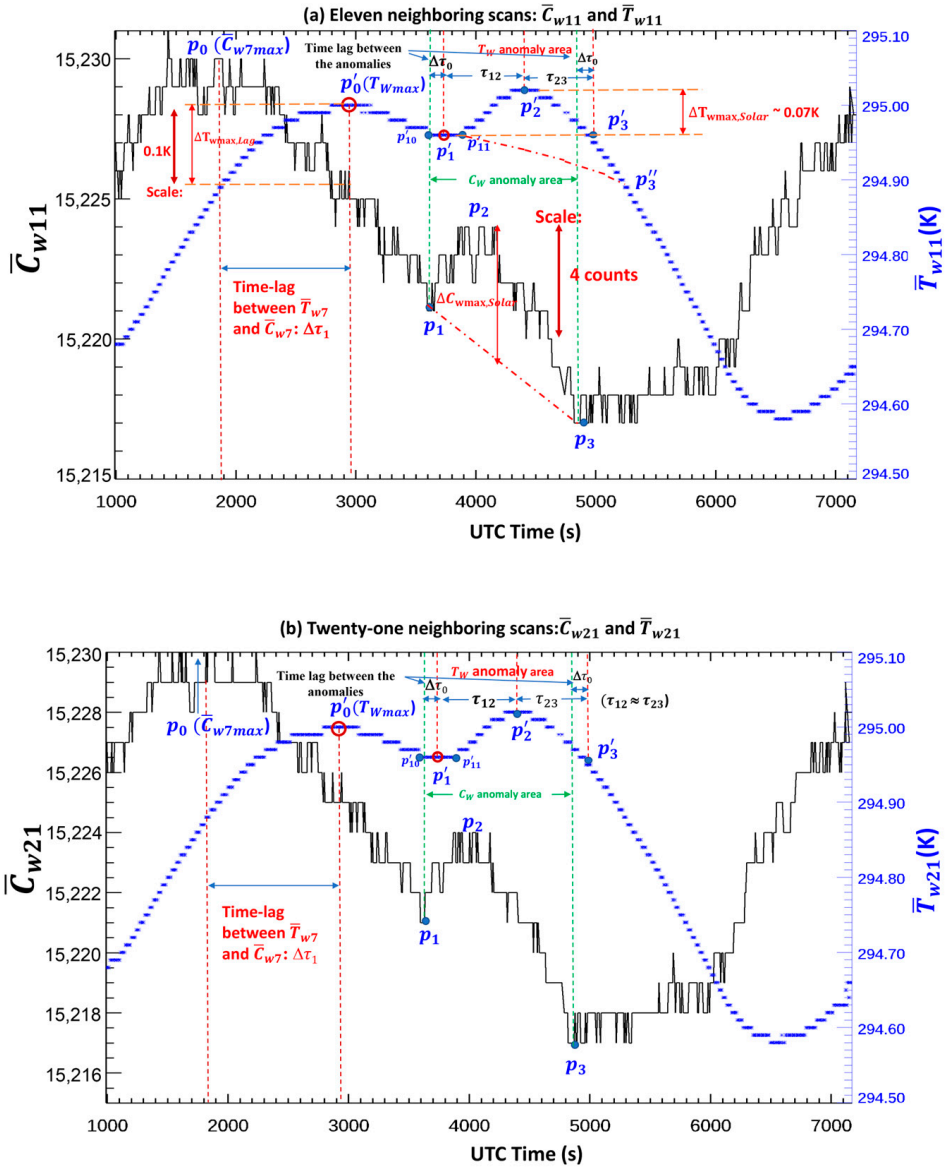

Figure 4. Time series of the weighted averaged blackbody target radiometric count $(\overline{C}_{wi}, i = 11, 21)$ and kinetic temperature $(\overline{T}_{wi})$ for Metop-C AMSU-A channel 1 during the first orbit of observations on 28 May 2021, using the two different neighboring scans in (2). In the figure, several positions are marked as a demonstration (not accurately) along with vertical dash lines to show the corresponding positions. For example, in (**a**), $\Delta C_{wmax,\mathrm{Solar}}$ and $\Delta T_{wmax,\mathrm{Solar}}$ approximately represent the maximum errors in warm count and kinetic temperature due to solar intrusion (see Section 5 for details), while $\Delta T_{wmax,Lag}$ denotes the maximum error in kinetic temperature due to the time lag. The descriptions of other positions are referred to those in Figure 3a. (**a**) $\overline{C}_{w11}$ and $\overline{T}_{w11}$. (**b**) $\overline{C}_{w21}$ and $\overline{T}_{w21}$.

Thirdly, more data sets are analyzed to understand whether those anomalous features constantly exist in each of the orbit AMSU-A data sets in channels 1 and 2. Figure 5 further presents the time series of T_W and C_W in channel 1 for four randomly selected days, denoting one day in each of the four seasons, i.e., 18 December 2019, 18 March 2020, 18 July 2020, and 18 September 2020. Hereinafter,$\overline{C}_{w7}$ is replaced by C_W to simplify our descriptions. Only one orbit of the data per day are plotted since the rest of the orbits have similar anomalous features for the same day. The features of channel 2 are similar to those of channel 1 (the figure is omitted).

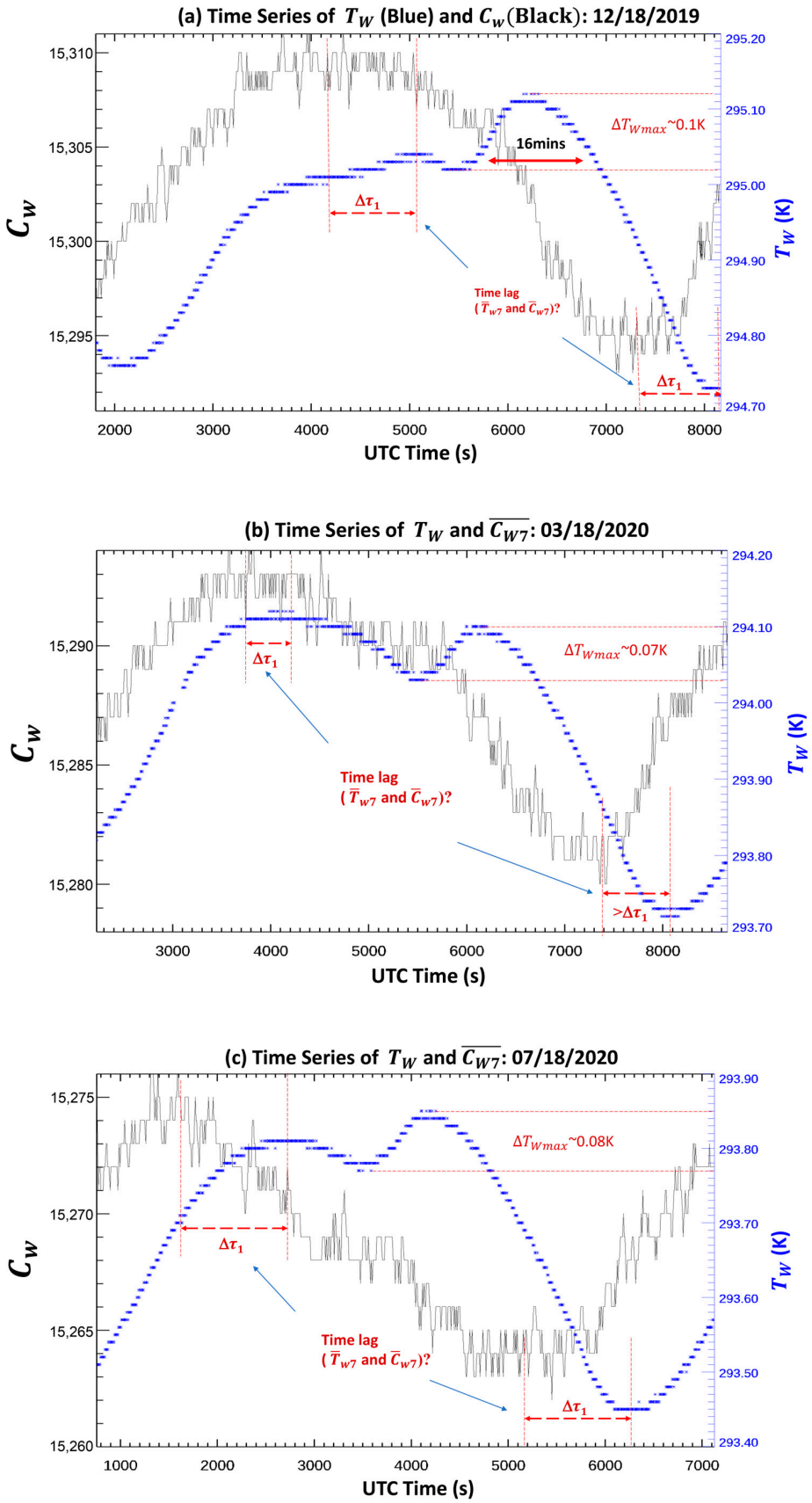

Figure 5. *Cont.*

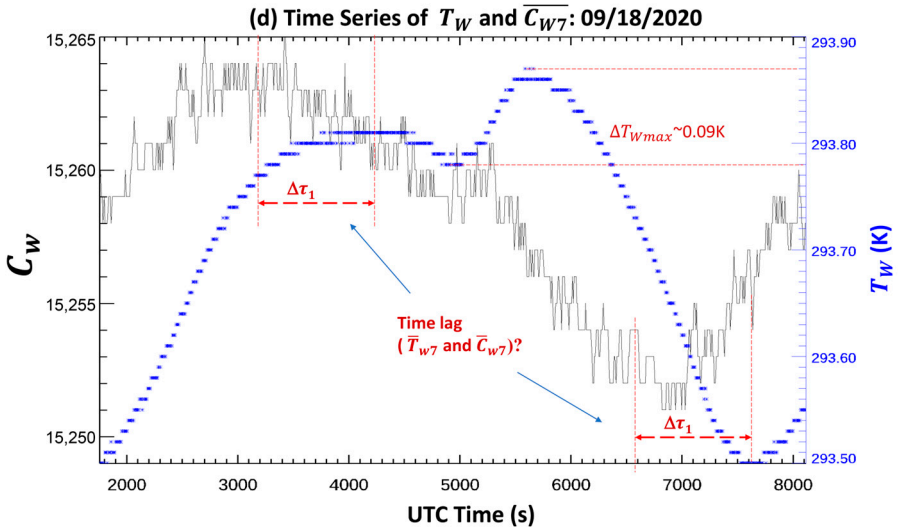

Figure 5. Time series of Metop-C AMSU-A channel 1 warm load count (C_w) (black color) and kinetic temperature (T_w) (blue color) by using one of the orbits of observations on four days. (**a**) 18 December 2019. (**b**) 18 March 2020. (**c**) 18 July 2020. (**d**) 18 September 2020. In the figure, a scale with 16 min is added to visually understand the time length of the anomalies, while $\Delta\tau_1$ is used to represent the time lag of the orbital variation of T_w behind that of C_w for a conceptual demonstration (not accurate). For simplification, the subscript 'Solar' have been removed from 'ΔC_{wmax} and ΔT_{wmax}' in the figure.

In view of the results in Figure 5, it is clearly found that the phenomena of the anomalous pattern and time lag constantly persist in both T_W and C_W for the four days. Certainly, the magnitude of the maximum anomaly pattern is slightly variable with the season. For instance, the maximum ΔT_{Wmax} (T_W anomaly) is about 0.1 K, 0.07 K, 0.08 K, and 0.09 K for the four days, respectively. For the C_W anomaly, its maximum magnitude is changed primarily from three to five counts, obviously affected by noise-caused fluctuations. The differences in magnitude should be related to changeable solar intrusion with the season and to the fluctuations. Regarding the anomaly pattern length, it is typically more than 16 min, even based on a conservative estimate as mentioned above. More data sets are analyzed in Section 3.2 below, leading to a similar conclusion.

To estimate the time lag of the orbital cycle of T_W behind that of C_W, we still use the two methods as mentioned above: the time difference between the normal maximum or the minimum positions in T_W and C_W in the absence of the anomaly. Approximate scales about the time difference are added in each of the figures. Generally, the resultant results are comparable using the two methods with an exception in Figure 5b. The time lag seems changeable with the season, with a long time around 18 min in summer and early fall (seen 18 July and 18 September 2020) and a short time down to about 9 min in winter and early spring (seen 18 March 2020). However, this conclusion is to be further validated since uncertainties remain in the current analysis. Moreover, we observe the time lag between the T_W and C_W anomalies for the data among the four different days, which is in a couple of minutes, further confirming the authenticity of the identified abnormal patterns and the time lag in the blackbody calibration target in channels 1 and 2 associated with the antenna unit A2.

Lastly, it is crucial to explore the feasibility of describing the abnormal patterns in both T_W and C_w using an appropriate polynomial function. Such an analysis will prove beneficial for our future studies, aiding in the development of an objective anomaly-correction algorithm for those issues. In this instance, we utilize data solely from the anomalous pattern occurring during the first orbit of 28 May 2021, to provide a demonstration of the viability of this concept. Figure 6a,b compare observed and fitted values about T_W and C_w in the data. We tested several degrees of polynomial functions to fit the variations of T_W and C_w with time. For the anomaly-contaminated T_W, the fourth degree of polynomial function

can provide the best fitting to the detected anomalous variation with an R-squared value up to 0.97. Other lower degrees of polynomial functions still can produce an R-squared value above 0.9 (see Figure 6a). However, for the anomaly-contaminated C_W, a higher degree of polynomial function can not obviously improve the fitting performance due to noise-caused high fluctuations in C_W (e.g., see Figure 3 above). A further smoothing for C_W should be first needed to reduce the impact of fluctuations on the fitting performance of the anomaly-contaminated data. Additional analyses are also needed in the future to develop a robust polynomial fitting algorithm about abnormal patterns in both T_W and C_w by covering different seasons of the anomaly-contaminated data.

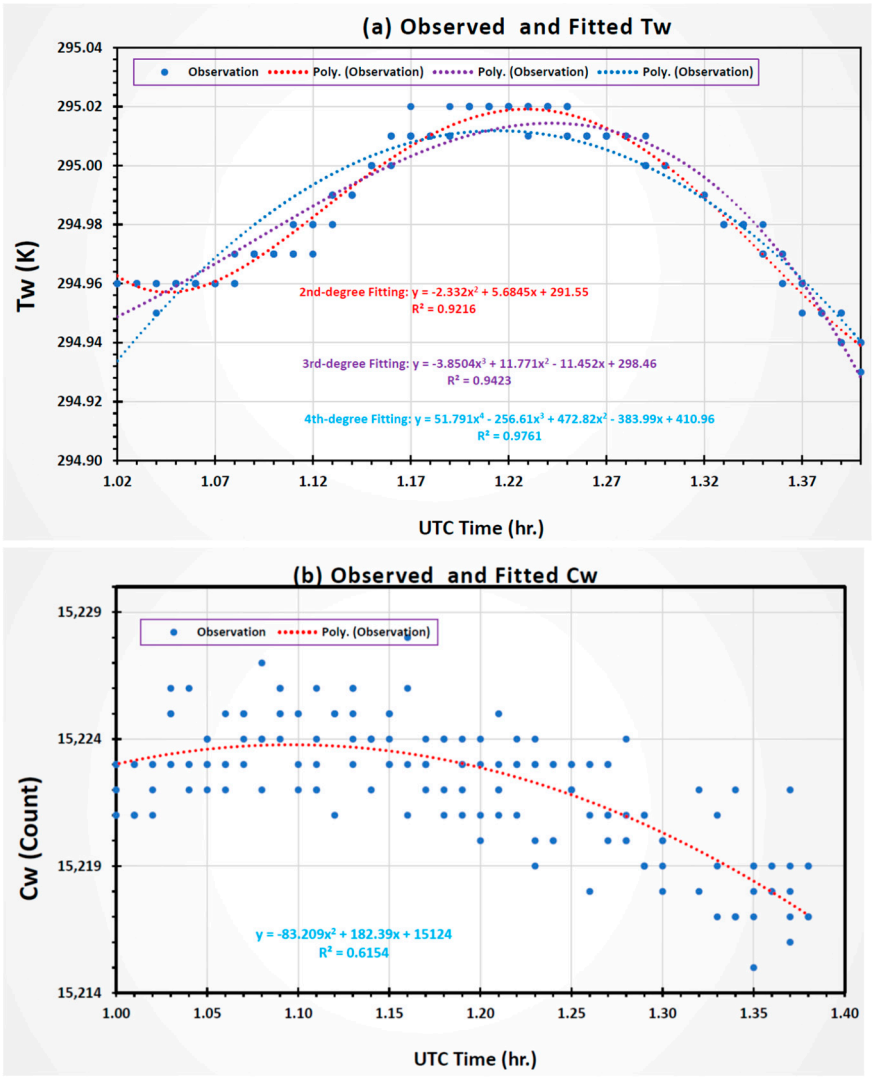

Figure 6. Comparison of observed and fitted values for the Metop-C AMSU-A channel 1 kinetic temperature (T_w) in (**a**) and warm load count (C_w) in (**b**). The data are anomaly-contaminated data in the first orbit on 28 May 2021. In the figure, three different degrees of polynomial functions are used to fit the variation of T_w with time, while only one degree of polynomial function is used to fit the variation of C_w with time. The fitting equations and R-squared values are also added in the figure.

In summary, two anomalous features in the blackbody calibration target in channels 1 and 2, namely abnormal pattern and time lag, have been found to persist consistently during each orbit. The anomalous pattern can last for more than 16 min during each orbit, with the blackbody kinetic temperature anomaly occurring a couple of minutes after the warm count anomaly. There is a good potential to describe the anomalous patterns associated with the blackbody kinetic temperature and warm count in a polynomial function, although

certain errors remain in fitting. Furthermore, the orbital variation of the blackbody kinetic temperature delays for a few minutes in comparison with that of the blackbody warm count. This indicates that the blackbody kinetic temperature responds more slowly to changes of the environmental temperature than the blackbody radiative temperature (warm count). However, uncertainties remain with our analysis, emphasizing the need for the development of a precise physical model about the anomaly and time lag problems through future studies.

4. Implication for Calibration Radiometric Accuracy

It is important to understand the possible impacts of the anomalous problems on the accuracy of AMSU-A TDR data. Currently, there are uncertainties in determining the anomalous increases (i.e., ΔC_w and ΔT_w) by using the above approximate method. Hence, this study only investigates the possibly largest implications of the problems during each orbit for the calibration accuracy of antenna temperatures in channels 1 and 2. According to our analysis, the anomalous pattern problem can have a larger impact on the calibration accuracy of the antenna temperature, so more assessments will be given to it here, while a simple assessment will be conducted for the time lag problem.

Generally, the impact assessment can be conducted using the two-point calibration equation in (1). For demonstration purposes, the chart in Figure 7 illustrates the calibration process in the absence/presence of the anomalous error ΔT_W. The nonlinearity effect is neglected in the chart because the contribution of the nonlinearity Q in (2) is usually less than one Kelvin (as reported in [33] for Metop-C AMSU-A). Moreover, the blackbody temperature operates within a relatively small dynamic range from orbit to orbit, and as a result, the nonlinearity effect at the blackbody temperature with a small variation is insignificant. In view of Figure 7, with a positive anomaly in T_w, point W shifts to point W', and the radiance R_s increases to R'_s due to a reduced slope CW' (i.e., the channel gain). Similarly, with a positive anomaly in C_w, the radiance R_s decreases due to an increased slope. Through the combined effect of two anomalies in T_w and C_w, the accuracy of radiance can be degraded.

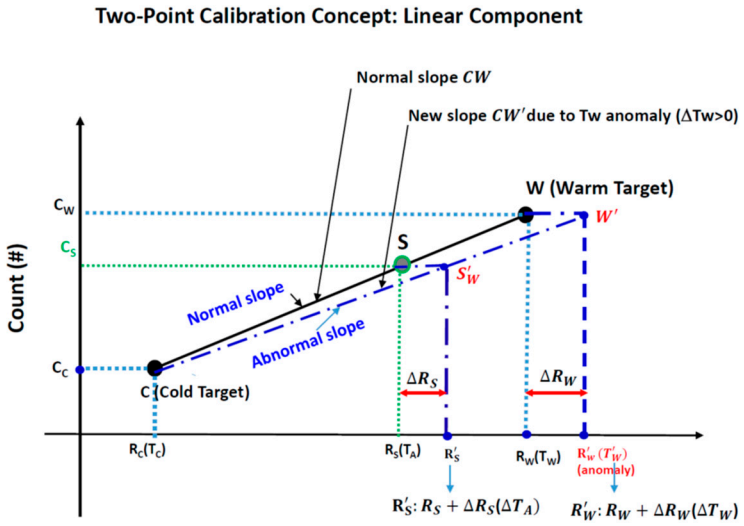

Figure 7. A conceptual chart of the two-point calibration process with/without errors in both C_w and T_w, where only the linear component is considered in the calibration. In the figure, the black line from point C to point W represents the two-point calibration process without errors, corresponding to normal blackbody PRT temperature T_w (R_w in the radiance domain), which leads to a correct Earth radiance R_S; the blue dash-dot line from point C to point W' represents the calibration process with an error (ΔT_W) in T_w, which leads to an errorneous Earth radiance R'_S; two double arrows denote the errors in radiance domain, ΔR_S and ΔR_w. Explanations for other dash lines and dot-dash lines are referred to the figure.

Mathematically, in the radiance domain, we can derive the error in Earth scene radiance in the presence of ΔC_w and ΔR_w by applying a derivative to (1) with respect to both R_w and C_w without the nonlinearity item Q. Then, approximately, we derive the following expression from it to estimate radiance errors in terms of errors in both R_w and C_w.

$$\Delta R_S \approx \frac{C_S - C_C}{C_w - C_C}(\Delta R_w - \frac{1}{G}\Delta C_w). \tag{5}$$

For end-users, the output corresponding to R_S is usually presented in temperature unit instead of radiance. To convert between radiance and temperature, the inverse of the Planck function is utilized. On the other hand, R_w is obtained from T_w via the Planck function [12]. Therefore, the antenna temperature error ΔT_A is discussed below instead of the radiance error, although the conversion from radiance to temperature is used in this analysis. Thus, (5) is re-written as follows:

$$\Delta T_A = -\frac{C_S - C_C}{C_w - C_C}\frac{1}{G_T}\Delta C_w + \frac{C_S - C_C}{C_w - C_C}\Delta T_w, \tag{6}$$

where G_T is the gain expressed in the domain of temperature to distinguish it from G that is expressed in in the domain of radiance (see (3) above). Additionally, the antenna temperature is denoted by using T_A instead of T_s since T_s is widely assumed to represent the surface temperature in various applications.

Firstly, for the anomalous pattern problem, which causes sudden and lasting increases in both C_w and T_w, i.e., ΔC_w and ΔT_w, theoretically, we can assume that

$$\Delta C_w = C_w^{OBS} - C_w^{fit}, \tag{7}$$

$$\Delta T_w = T_w^{OBS} - T_w^{fit}, \tag{8}$$

where the superscript '*OBS*' and '*fit*' represent the measurement and fitted values, respectively, for each of T_w and C_w during the anomalous period.

C_w^{fit} and T_w^{fit} represent the anomaly-free warm count and kinetic temperature of the blackbody target, respectively, during the solar contamination. However, we do not have the truth about the anomaly-free warm count and kinetic temperature of the blackbody target during each orbit. To understand the possibly largest impact of the anomalies during each orbit, we make an approximate estimate about them by using linear fitting with the assumption that $\Delta T_w = 0.0$ and $\Delta C_w = 0.0$ at the two edge points of the abnormal patterns.

By using Figure 4a as an example, two pairs of points (p_1, p_2) and (p_1', p_2') represent two edge points for the C_w and T_w anomalous patterns in the first orbit of the data on 28 May 2021. It is conservatively estimated that the maximum abnormal increase in C_w (denoted as $\Delta C_{wmax,\text{Solar}}$ in the figure) is about four counts, while that in T_w (denoted as $\Delta T_{wmax,\text{Solar}}$) is about 0.07 K, as discussed in Section 3 above. According to (6), for the data in channel 1 in Figure 4a, the resultant maximum radiance error due to $\Delta C_{wmax,\text{Solar}}$, which is denoted as $\Delta T_{Amax}^{\Delta C_w}$, is approximately 0.16 K, and the radiance error due to $\Delta T_{wmax,\text{Solar}}$, which is denoted as $\Delta T_{Amax}^{\Delta T_w}$, is about 0.05 K. Similar radiance errors exist in channel 2. Notice that the overall maximum radiance error (ΔT_{Amax}) due to the anomaly pattern issue is a combined impact of $\Delta C_{wmax,\text{Solar}}$ and $\Delta T_{wmax,\text{Solar}}$ through (6), where each of them has a different sign, as described in (6). As estimated above, the radiance error due to $\Delta C_{wmax,\text{Solar}}$ is much larger than that due to $\Delta T_{wmax,\text{Solar}}$, so the overall radiance errors are dominated by $\Delta C_{wmax,\text{Solar}}$.

Certainly, the magnitudes of both $\Delta C_{wmax,\text{Solar}}$ and $\Delta T_{wmax,\text{Solar}}$ within the anomalous pattern can change slightly with an updated ending position of the anomaly or a different fitting method. For instance, $\Delta T_{wmax,\text{Solar}}$ could be on the order of 0.1 K, which is bigger than our current estimate, if the anomaly ended at the point p_3'' instead of p_3', which might be more reasonable (see Figure 4a). Hence, this study only provides conservative estimates for the largest anomalous increases within the two anomalous patterns. Due to

the important impact of the anomalous pattern problem, a similar assessment is applied to 25 days of the data sets spanning 2 years. Figure 8a,b provide the daily-averaged largest radiance errors (absolute value) at the two channels for $\Delta T_{Amax}^{\Delta C_w}$, $\Delta T_{Amax}^{\Delta T_w}$ and ΔT_{Amax}, respectively. Generally, the daily averaged radiance errors from each of the anomalies primarily distribute in a range from 0.04 K to 0.07 K for $\left|\Delta T_A^{\Delta T_w}\right|_{max}$ and in the range from 0.15 K to 0.25 K for $\left|\Delta T_A^{\Delta C_w}\right|_{max}$. The combined radiance errors, ΔT_{Amax}, vary in the range from 0.14 K to 0.24 K, depending on orbit, season, and channel.

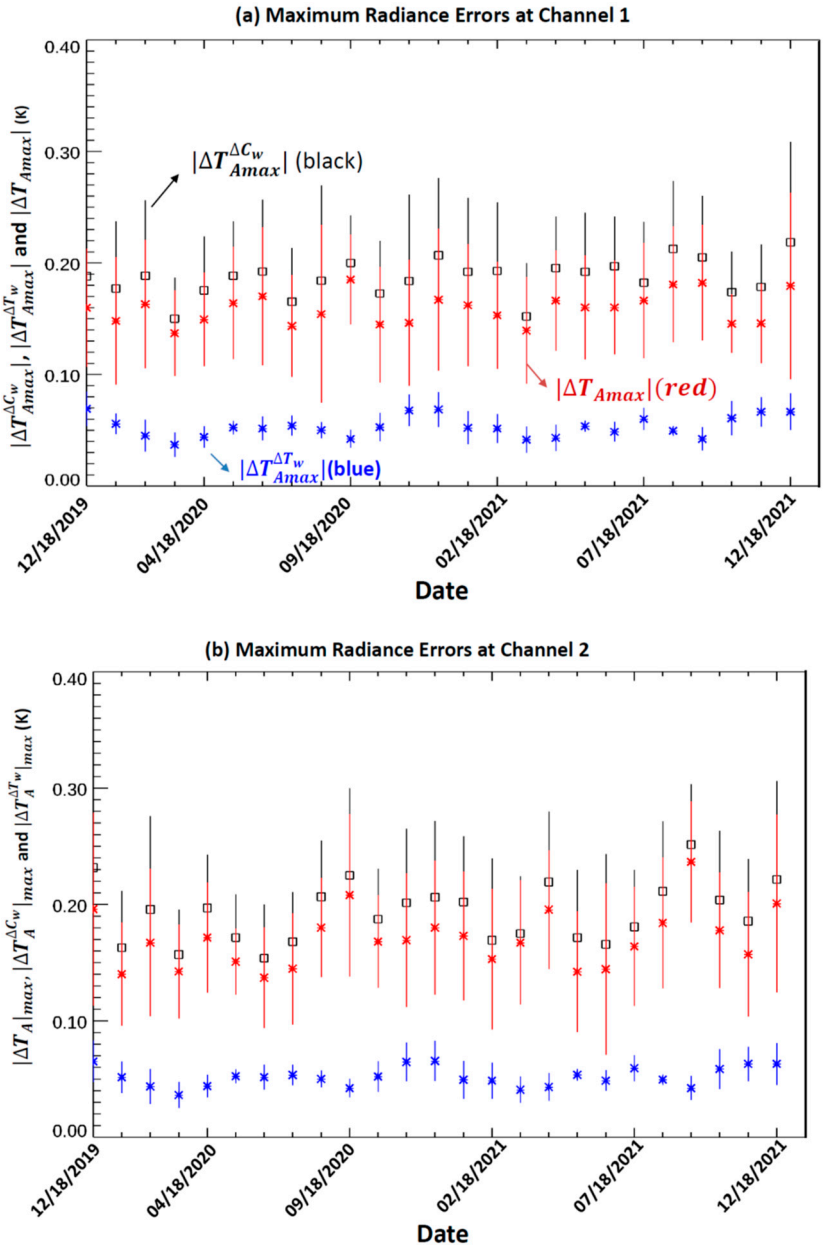

Figure 8. Daily-averaged largest radiance errors (absolute value) for $\Delta T_{Amax}^{\Delta C_w}$, $\Delta T_{Amax}^{\Delta T_w}$ and ΔT_{Amax} separately for the Metop-C AMSU-A TDR data set in channels 1 and 2, i.e., $\left|\Delta T_{Amax}^{\Delta C_w}\right|$ (black color), $\left|\Delta T_{Amax}^{\Delta T_w}\right|$ (blue color) and $|\Delta T_{Amax}|$ (red color). The data sets cover one day per month from 18 December 2019 through 18 December 2021; the daily mean is computed by averaging all maximum radiance errors (absolute value) per orbital anomaly event in a day. The figure includes the standard deviation among orbits in a day (indicated by a vertical line per the daily mean). (**a**) Channel 1. (**b**) Channel 2.

Table 3 presents the averaged maximum antenna temperature errors due to various error sources and the corresponding standard deviations for channels 1 and 2, which are derived from the entire test data sets used in Figure 8. Evidently, despite seasonal fluctuations, the warm count error source, $\overline{|\Delta T_{Amax}^{\Delta C_w}|}$, is the predominant factor contributing to radiance errors, surpassing the influence of the blackbody kinetic temperature error source.

Table 3. Averaged maximum antenna temperature errors due to various error sources and the corresponding standard deviations for channels 1 and 2, derived from the entire test data sets used in Figure 8.

Channel Index	T_A Error Due to $\Delta C_{wmax,\mathrm{Solar}}$ (K)		T_A Error Due to $\Delta T_{wmax,\mathrm{Solar}}$ (K)		T_A Error Due to Both $\Delta C_{wmax,\mathrm{Solar}}$ and $\Delta T_{wmax,\mathrm{Solar}}$ (K)	
	$\overline{\lvert \Delta T_{Amax}^{\Delta C_w} \rvert}$	σ_1	$\overline{\lvert \Delta T_{Amax}^{\Delta T_w} \rvert}$	σ_2	$\overline{\lvert \Delta T_{Amax} \rvert}$	σ_3
1	0.22	0.09	0.05	0.01	0.16	0.05
2	0.19	0.06	0.05	0.01	0.17	0.05

Notes: (1). $\overline{|\Delta T_{Amax}^{\Delta C_w}|}$, $\overline{|\Delta T_{Amax}^{\Delta T_w}|}$, and $\overline{|\Delta T_{Amax}|}$ denote the average of all daily-averaged maximum antenna temperature errors with regard to the largest anomalies in C_w, T_w and both of them, respectively. (2). σ_1, σ_2, and σ_3 represent the standard deviations from $\overline{|\Delta T_{Amax}^{\Delta C_w}|}$, $\overline{|\Delta T_{Amax}^{\Delta T_w}|}$, and $\overline{|\Delta T_{Amax}|}$ separately. (3). The explanations of $\Delta C_{wmax,\mathrm{Solar}}$ and $\Delta T_{wmax,\mathrm{Solar}}$ are referred to Figure 4 above.

Secondly, for the time lag problem in the T_w orbital cycle in comparison to the C_w cycle, a simple impact assessment is performed here. The error in C_w is reasonably assumed to be zero since the time lag is defined against the orbital cycle of C_w. So, the impact on the calibration accuracy of T_A is determined by the error in T_w due to the time lag, i.e., $\Delta T_A = \frac{C_S - C_C}{C_w - C_C} \Delta T_w$. Generally, the T_w varies by a small variation (~0.4 K) during each orbit, and the maximum error in T_w (denoted as $\Delta T_{wmax,\,Lag}$ in the figure) due to the time lag is only in the order of 0.1 K. A conceptual demonstration is added in Figure 4a, which uses 11 neighboring scans for the average, since Figure 3a has been crowded with multiple notes or lines. The resulting maximum error in T_A per orbit is in the order of 0.08 K, changing with the magnitudes of C_S, C_C, and C_w. Certainly, for most of the data during the orbit, the resulting T_A error should be much smaller than this. In addition, the errors during most of the orbit might fall within the range of the instrument's noise level. This might partly explain why the radiance errors resulting from this entire time lag were not identified in previous calibration studies of AMSU-A instruments.

It is important to mention that the magnitudes of the radiance errors are computed without taking into account instrument noise. In practice, the AMUS-A instrument always exhibits a certain level of noise in its measurements [10,11,14], which is quantified by NEDT. Traditionally, the onboard AMSU-A NEDT has been determined simply based on the standard deviation of warm counts per orbit [5]. Other methods are also applicable by further including noise contribution from other calibration parameters, which can result in small differences in magnitude [10,14,36,37]. The estimated NEDT values for channels 1 and 2 are approximately 0.18 K, referring to the ICVS web-based monitoring system in https://www.star.nesdis.noaa.gov/icvs/status_MetOPC_AMSUA.php, accessed on 5 April 2019. Therefore, this NEDT introduces an additional uncertainty up to 0.18 K to the above-estimated radiance errors.

Therefore, the calibration accuracy of the AMSU-A antenna temperature in channels 1 and 2 can be affected by the anomalous pattern problem and the overall time lag in the T_w orbital cycle in comparison to the C_w orbital cycle. Particularly, the warm count anomaly can lead to the largest radiance errors approximately from 0.14 K to 0.24 K. This estimate can be affected by instrument noise. Therefore, it is necessary to investigate the root cause to the warm count anomaly along with the kinetic temperature anomaly in the following section. The root cause to the overall time lag of the T_w orbital cycle is deferred to future studies when it is well understood.

5. Root Cause Analysis of the Anomalous Pattern Problem

Previous studies on AMSU-A calibration parameters have typically focused on short-term and long-term stabilities, as seen in references [9,12,13], while the long-term trends of those parameters for all 15 AMSU-A channels are routinely monitored in the NOAA ICVS web site (https://www.star.nesdis.noaa.gov/icvs/index.php, accessed on 6 June 2012). The abnormal patterns in T_w and C_w were not addressed in previous studies. Although there is no known reference for the AMSU-A, a solar anomalous effect was reported as early as 1998 for the AVHRR instrument flown in the NOAA polar orbiting satellites. The AVHRR instrument suffered from solar contaminations when exposed to sunlight at spacecraft sunrise, which was related to a large scan angle within the AVHRR observations. The AMSU-A instrument also has a large scan angle, which increases the technical risk of solar intrusion to the AMSU-A2 blackbody calibration target. Moreover, other established facts below support the existence of solar intrusion, as described below.

Firstly, the fact that solar intrusion is the root cause of the AMSU-A2 calibration anomaly is supported by the orbital simulation for Metop-C AMSU-A observations through consistent occurrence time and solar angle position. The orbital simulation was performed using the physics-based and industry standard software package Satellite Toolkit (STK) version 11.5. STK has many modules and uses several physical models, and the model used in this study was the Simplified General Propagation model (SGP4). SGP4 was initially published along with sample code in 1988 and further refined over time [38] for accurately predicting the position of a satellite at any given time with the TLE (Two-Line Elements) provided by NORAD (North American Aerospace Defense Command). Specifically, it can calculate the solar angles at the spacecraft and AMSU-A instrument at the exact time of the selected orbit using the "Two-Line-Elements" (TLEs), with the industry standard STK or Satellite Toolkit. The calculated information also includes the time of the satellite sunrise and sunset based on the solar angles at the spacecraft. The SGP4 prediction accuracy is around 1 km on the Earth with the most up-to-date TLEs which are released daily (available from https://www.celestrak.com, accessed on 1 January 1986) [39]. Therefore, the orbital simulation can provide a very realistic scenario of the satellite position in relation to the Earth, Sun, and instrument on the Metop-C satellite.

Figure 9a is the orbit simulation for the first orbit of the AMSU-A observations on 28 May 2021. According to the orbit simulation results, two satellite terminator times, i.e., the time of satellite sunset and sunrise, happen in 1:09 UTC and 1:41 UTC, respectively, for the selected orbit, which is also added in the figure. Note that the abovementioned abnormal pattern in C_w during the same orbit happens approximately from 1:02 UTC to 1:19 UTC with uncertainty of about 1 min, with the peak at a time close to the sunset time, seen in Figure 4 above. In other words, the solar contamination impact takes place when the spacecraft is in proximity to the satellite terminator roughly 7–8 min prior to spacecraft sunset. Regarding an additional more than 8 min of anomalous pattern, it is a cooling process from the abnormally increased peak to zero that is associated with the thermal conductivity characteristics of the blackbody target. However, further study is needed to quantify this cooling process. Therefore, the starting and peaking positions of the anomalous pattern are consistent with the satellite position relative to the Sun in the orbit simulation. This consistency shows that solar intrusion can be the root cause of the AMSU-A2 calibration anomaly.

Secondly, the specific structure of the AMSU-A instrument confirms the feasibility of the solar intrusion. Within the AMSU-A instrument, the warm load targets were designed to be surrounded by a metal shroud to prevent stray radiation from external sources [34,40]. In fact, the above-mentioned anomalous features were not observed in pre-launch in the Metop-C AMSU-A instrument. This fact implies that the design of AMSU-A is mostly reasonable. However, it should be challenging to capture solar intrusion issue since the ground experiments for AMSU-A instruments were made under limited circumstances. It is possible that the on-orbit warm load shroud could not be perfectly mated in all directions with the shroud surrounding the rotating reflector antenna. Especially, AMSU-A

instrument has a large scan angle of 96.66°, as shown in Figure 9b about the AMSU-A scan geometry. This large scan angle likely offers an easy entrance to sunlight under certain large SZA circumstances.

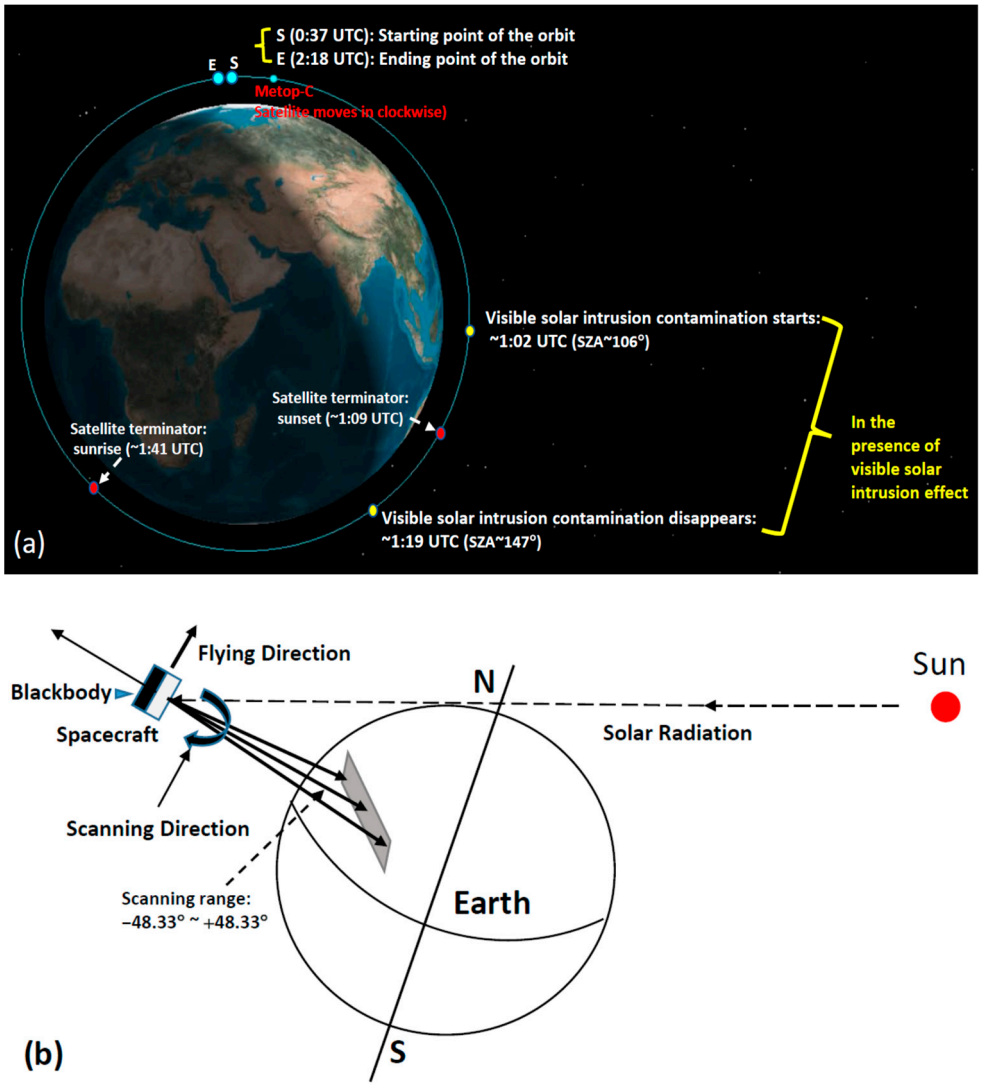

Figure 9. (**a**) Metop-C/AMSU-A orbit simulation (28 May 2021, Sunset at ~1:09 UTC and Sunrise at ~1:41 UTC), where the positions of S (0:37 UTC) and E (2:18 UTC) correspond to the starting and ending points of the simulated orbit. The positions of Sunset and Sunrise are approximately marked in the orbit simulation (not accurate). (**b**) AMSU-A geometry sketch along with Sun and Earth (not to scale).

Thirdly, the solar intrusion to the blackbody target is confirmed by a similar feature in instrument temperature (T_{Shelf}) associated with the AMSU-A2 channels. Figure 10 displays the time series of the AMSU-A2 T_{Shelf}, where T_w is included for comparison. According to the analysis of the T_w anomaly, the solar radiance contamination remains primarily from the point p'_1 to the point p'_3 with a peak around the point p'_2. Obviously, during this period, the T_{Shelf} also exhibits a relatively rapid increase (a positive anomaly), which further confirms the presence of extraneous radiance rather than a warm load calibration source.

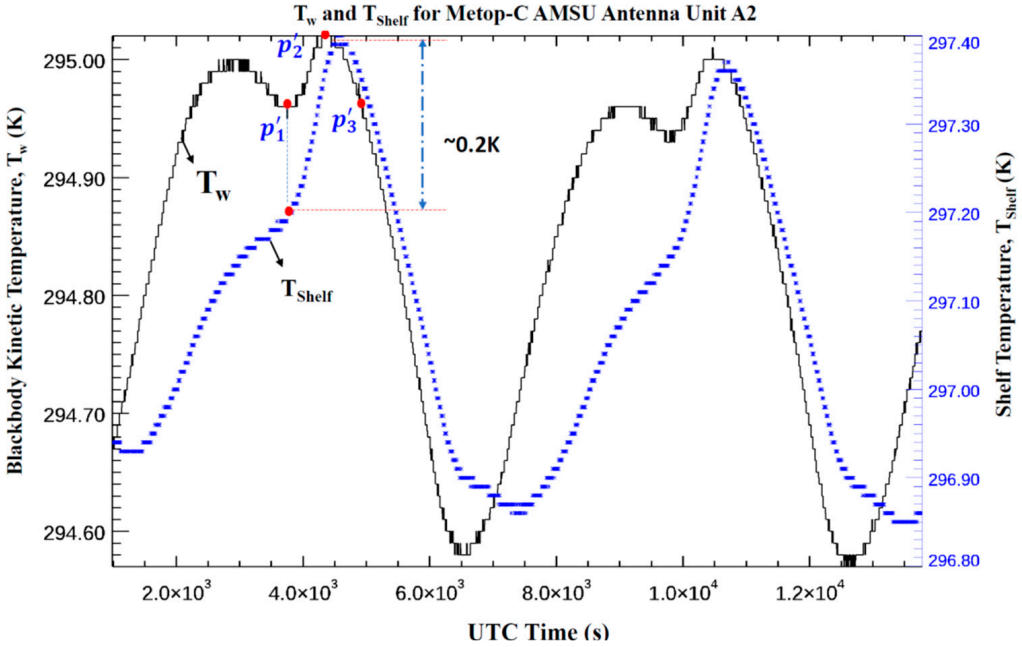

Figure 10. Time series of Metop-C AMSU-A2 blackbody kinetic temperature (T_w) (black color) and the instrument shelf temperature $\left(T_{Shelf}\right)$ (blue color) within two orbits of observations, where the data are on 28 May 2021. The points from p_1' to p_3' approximately represent the positions of the starting, peaking, and minimum anomalies in T_w during the first orbit of observations.

Furthermore, solar intrusion happens on each orbit of AMSU-A observations in channels 1 and 2, which is confirmed by the analysis in the previous section. A follow-up question is whether solar intrusion at each orbit always occurs under circumstances with large SZAs. The position of solar contamination is theoretically a function of many factors, including instrument alignment within the satellite, orbit, season, and time, as described for the AVHRR solar contamination [28]. However, we lack this information from either pre-launch or flight measurements to establish a solid physical model for this analysis. While this study did not yield precise values for the starting and ending positions of the anomalies including corresponding SZA due to lack of sufficient information, we have determined approximate estimates for these parameters based on observable and abnormal increases in both T_w and C_w (see the analysis in Section 3.1 above). The analysis has been further applied to 25 days of the Metop-C AMSU-A data sets spanning 2 years in channels 1 and 2 used in Figure 8 (Section 4 above). Through the analysis, the SZA values with the starting and ending positions of the anomalies in T_w can be obtained from the AMSU-A TDR data. As shown in Figure 11, the magnitudes of SZAs are typically larger than 95°. Additionally, both starting and ending SZAs display a stable semi-annual or annual pattern. For example, the daily-averaged starting SZA shows a maximum of 107° typically in February and September, and a minimum of 102° in May (June) and November (December). The daily-averaged ending SZA behaves in an annual pattern, reaching the peak of 149° typically in June and the lowest of 138° in February. Overall, all orbital anomaly events during two years are found to occur under large SZAs with a minimum of 95°. Table 4 presents the averaged SZA values at the starting and ending positions of the detected anomalies in T_w for the entire anomalous events depicted in Figure 11. So, the averaged affected regions by solar intrusion cover the variation of about 40° in SZA, with an averaged uncertainty less than 2°.

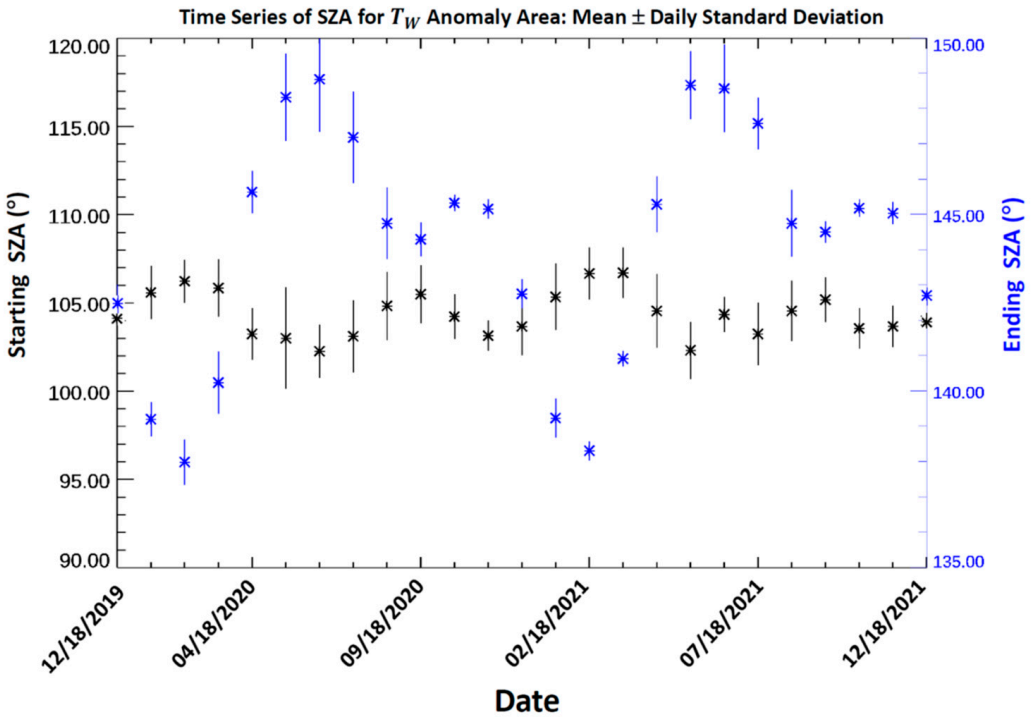

Figure 11. Time series of daily averaged SZA for the starting (see left y-axis) and ending (see right y-axis) positions for the orbital anomaly events in T_w. The date covers two annual cycles by including one day per month from 18 December 2019 to 18 December 2021. The vertical variation above/below each daily average represents the standard deviation (σ) of SZA for the daily mean.

Table 4. Averaged Solar Zenith Angle (SZA) values at the starting and ending positions of the detected anomaly in T_w for all abnormal events depicted in Figure 11.

Starting SZA (°)		**Ending SZA (°)**	
$\overline{\theta_{start}}$	σ_4	$\overline{\theta_{end}}$	σ_5
104.35	1.53	144.12	0.67

Notes: (1). $\overline{\theta_{start}}$ and $\overline{\theta_{end}}$ represents the averaged starting and ending SZAs, respectively, in the presence of the anomalous patterns in T_w across the whole data sets. (2). σ_4 and σ_5 denote the averaged uncertainty of all daily-averaged SZAs from $\overline{\theta_{start}}$ and $\overline{\theta_{end}}$, respectively.

Therefore, the above facts demonstrate that solar illumination is accountable for the anomalies in both the radiative temperature (C_w) and kinetic temperature (T_w) observed in the AMSU-A blackbody target associated with the antenna unit A2. This assertion is supported through the Metop-C AMSU-A orbit simulation, the AMSU-A sensor structure design, the AMSU-A2 instrument shelf temperature (T_{Shelf}) anomaly, the specific occurrence circumstances with large SZAs, and similar SZA regions during each of the orbits in a day.

6. Summary and Conclusions

This study presents the first discovery of both the solar intrusion-caused anomalous pattern and the time lag problems on the Metop-C AMSU-A data in channels 1 and 2 associated with the antenna unit A2. The anomalous pattern is characterized by abnormal increases in both C_w and T_w, typically lasting for more than 16 min during each orbit of satellite observations. The peaking anomalous increase during each orbit varies approximately from three to five counts for C_w and from 0.06 to 0.1 K for T_w, depending upon orbit, season, and channel. By analyzing 25 days of the data spanning 2 years from 18 December 2019 through 18 December 2021, the resultant maximum antenna temperature

errors due to abnormal increases in C_w are characteristically in the range from 0.15 K to 0.25 K, which dominated the radiance error during the abnormal pattern period, since the maximum errors due to the abnormal increase in T_w are in the range approximately from 0.04 K to 0.07 K. The combined largest radiance errors vary approximately from 0.14 K to 0.24 K, depending upon orbit, season, and channel. Regarding the time lag problem, the orbital variation of T_w has a delay typically of more than 9 min in comparison with that of C_w, which can cause an antenna temperature error up to 0.1 K. Hence, this study underscores the imperative need in future study to rectify radiance errors to reconstruct a more accurate long-term Metop-C AMSU-A radiance data set in channels 1 and 2, especially for climate studies.

Furthermore, this study further investigates the solar intrusion on the blackbody calibration target in channels 1 and 2, which is the root cause of the abnormal patterns in C_w and T_w. Solar illumination is constantly observed during each orbit near the satellite terminator, and its impact occurs in close proximity to the satellite terminator a few minutes before spacecraft sunset, and this influence can persist for a few additional minutes after spacecraft sunrise. Solar contamination results in a blackbody calibration problem for channels 1 and 2 within each orbit, manifesting as abrupt increases in kinetic temperature and radiative temperature (warm count) of the AMSU-A2 blackbody calibration target. Solar intrusions typically occur under circumstances with solar zenith angles above 95°. Moreover, solar intrusion leads to abrupt increases in AMSU-A2 shelf temperature.

While this study has undertaken an initial assessment of the anomalous pattern problem, including the feasibility of fitting these anomalous patterns using polynomial functions, and has identified the root cause (solar contamination) and resultant radiance calibration errors, it is essential to acknowledge that several uncertainties persist in the analysis. For example, the determination of the occurrence of each anomaly event in either C_w or T_w relies on an approximation. This approximation assumes the T_w anomaly effect during each orbit is symmetric, where the duration from the onset of the anomaly to its peak is equivalent to the duration from the peak to the conclusion of the anomaly. The results have shown that the T_w for a few scan lines after the derived termination of the anomaly is still not smooth. This suggests that the current approximations used in this study might underestimate the impact of the anomaly. Additionally, the C_w and T_w anomalies are estimated in this study based on a linear fitting approximation for the anomaly-free C_w and T_w. These approximations might under/overestimate slightly magnitudes of ΔC_w and ΔT_w including their peak values. Finally, we have not investigated the root cause to the time lag problem.

Overall, the discoveries in this study necessitate further research to reconstruct Metop-C AMSU-A2 TDR data by mitigating the radiance errors due to the solar intrusion effect and the time lag problem. The outcomes of this study hold significance for the analysis of solar contamination in the AMSU-A2 unit aboard the NOAA-18, NOAA-19, Metop-A, and Metop-B, where solar intrusion is partially present.

Author Contributions: Conceptualization, B.Y.; software, B.Y.; validation, B.Y., C.C. and N.S.; formal analysis, B.Y.; investigation, B.Y.; resources, B.Y.; data curation, B.Y.; writing—original draft preparation, B.Y.; writing—review and editing, B.Y. and C.C.; visualization, B.Y.; supervision, B.Y.; project administration, B.Y.; funding acquisition, B.Y. All authors have read and agreed to the published version of the manuscript.

Funding: This research received no external funding.

Data Availability Statement: The operational Metop-C AMSU-A TDR data sets are available in the NOAA Comprehensive Large Array-data Stewardship System (CLASS) through the following link: https://www.avl.class.noaa.gov/release/data_available/tovs_atovs/index.htm, accessed on 1 June 2019.

Acknowledgments: The authors would like to thank the NOAA Center for Satellite Applications and Research (STAR) for supporting NOAA legacy Advanced Microwave Sounding Unit-A (AMSU-A) instrument calibration/validation. Thanks go to Junye Chen for his effort in activities of the Metop-C AMSU-A calibration and validation. Thanks go to Cheng-zhi Zou and a few anonymous reviewers for giving many valuable comments in improving the quality of the manuscript. A big thanks also goes to Douglas Howard and a few other anonymous reviewers for giving valuable comments.

Conflicts of Interest: Ninghai Sun is employed by the company Global Science Technologies Inc. The remaining authors declare that the research was conducted in the absence of any commercial or financial relationships that could be construed as a potential conflict of interest.

Disclaimer: The manuscript contents are solely the opinions of the author(s) and do not constitute a statement of policy, decision, or position on behalf of NOAA or the U. S. Government.

References

1. Northrop Grumman Electronic Systems (NGES). *AMSU-A System Operation and Maintenance Manual for METSAT/METOP, S/N 105 through 109*; Technique Report NAS 5-32314 CDRL 307; NGES: Linthicum Heights, MD, USA, 2010.
2. Northrop Grumman Electronic Systems (NGES). *Calibration Log Book for the Advanced Microwave Sounding Unit-A (AMSU-A)*; Report #10481A; Aerojet: Azusa, CA, USA, 1995.
3. Northrop Grumman Electronic Systems (NGES). *Calibration Log Book for AMSU-A2 SN 107*; Report No. 15267; Northrop G Grumman: Azusa, CA, USA, 2008; p. 91702.
4. Mo, T.; Weinreb, M.; Grody, N.; Wark, D. *AMSU-A Engineering Model Calibration*; NOAA Technical Report NESDIS 68; NOAA: Silver Spring, MD, USA, 1993.
5. Mo, T. Prelaunch calibration of the Advanced Microwave Sounding Unit-A for NOAA-K. *IEEE Trans. Microw. Theory Technol.* **1996**, *44*, 1460–1469. [CrossRef]
6. Mo, T. AMSU-A Antenna Pattern Corrections. *IEEE Trans. Geosci. Remote Sens.* **1999**, *37*, 103–112.
7. Mo, T. *Calibration of the Advanced Microwave Sounding Unit-A Radiometer for MetOp-A*; NOAA Technical Report NESDIS 121; United States Department of Commerce: Washington, DC, USA, 2006.
8. Mo, T.; Kigawa, S. A study of lunar contamination and onorbit performance of the NOAA-18 Advanced Microwave Sounding Unit-A. *J. Geophys. Res.* **2007**, *112*, D20124. [CrossRef]
9. Mo, T. Postlaunch calibration of the MetOp-A Advanced Microwave Sounding Unit-A. *IEEE Trans. Geosci. Remote Sens.* **2008**, *46*, 3581–3600. [CrossRef]
10. Tian, M.; Zou, X.; Weng, F. Use of Allan Deviation for Characterizing Satellite Microwave Sounder Noise Equivalent Differential Temperature (NEDT). *IEEE Geosci. Remote Sens. Lett.* **2015**, *12*, 2477–2480. [CrossRef]
11. Yan, B.; Wu, X.; Chen, J.; Ahmad, K.; Kireev, S.; Qian, H.; Zou, C.-Z.; Cao, C. Metop-C AMSU-A and AVHRR Sensor Data Recorder (SDR) Data Calibration/Validation (CalVal): Status & Prospective. In Proceedings of the 2019 Conference on Characterization and Radiometric Calibration for Remote Sensing, Logan, UT, USA, 21–24 August 2019. Available online: https://digitalcommons.usu.edu/cgi/viewcontent.cgi?article=1358&context=calcon (accessed on 1 September 2019).
12. Yan, B.; Chen, J.; Zou, C.-Z.; Ahmad, K.; Qian, H.; Garrett, K.; Zhu, T.; Han, D.; Green, J. Calibration and Validation of Antenna and Brightness Temperatures from Metop-C Advanced Microwave Sounding Unit-A (AMSU-A). *Remote Sens.* **2020**, *12*, 2978. [CrossRef]
13. Yan, B.; Ahmad, K. Derivation and Validation of Sensor Brightness Temperatures for Advanced Microwave Sounding Unit-A Instruments. *IEEE Trans. Geosci. Remote Sens.* **2020**, *59*, 404–414. [CrossRef]
14. Yan, B.; Kireev, S.V. A New Methodology on Noise Equivalent Differential Temperature Calculation for On-Orbit Advanced Microwave Sounding Unit—A Instrument. *IEEE Trans. Geosci. Remote Sens.* **2021**, *59*, 8554–8567. [CrossRef]
15. Derber, J.C.; Wu, W.S. The use of TOVS cloud-cleared radiances in the NCEP SSI analysis system. *Mon. Weather Rev.* **1998**, *126*, 2287–2299. [CrossRef]
16. Zhu, T.; Zhang, D.-L.; Weng, F. Impact of the Advanced Microwave Sounding Unit Measurements on Hurricane Prediction. *Mon. Weather. Rev.* **2002**, *130*, 2416–2432. [CrossRef]
17. Kelly, G.; Thépaut, J.-N. *Evaluation of the Impact of the Space Component of the Global Observation System through Observing System Experiments*; ECMWF Newsletter, No. 113; ECMWF: Reading, UK, 2007; pp. 16–28. Available online: https://www.ecmwf.int/sites/default/files/elibrary/2007/17527-evaluation-impact-space-component-global-observing-system-through-observing-system-experiments.pdf (accessed on 1 December 2007).
18. Zou, X.L.; Qin, Z.; Weng, F. Impacts from assimilation of one data stream of AMSU-A and MHS radiances on quantitative precipitation forecasts. *Q. J. R. Meteorol. Soc.* **2017**, *143*, 731–743. [CrossRef]
19. Weng, F.; Zhao, L.; Ferraro, R.R.; Poe, G.; Li, X.; Grody, N.C. Advanced microwave sounding unit cloud and precipitation algorithms. *Radio Sci.* **2003**, *38*, 8086–8096. [CrossRef]
20. Zhu, T.; Weng, F. Hurricane Sandy warm-core structure observed from advanced Technology Microwave Sounder. *Geophys. Res. Lett.* **2013**, *40*, 3325–3330. [CrossRef]

21. Tian, X.; Zou, X. ATMS- and AMSU-A-derived hurricane warm core structures using a modified retrieval algorithm. *J. Geophys. Res. Atmos.* **2016**, *121*, 12630–12646. [CrossRef]
22. Zou, X.L. Climate trend detection and its sensitivity to measurement precision. *Adv. Meteorol. Sci. Technol.* **2012**, *2*, 41–43.
23. Zou, C.Z.; Wang, W. Intersatellite calibration of AMSU-A observations for weather and climate applications. *J. Geophys. Res. Atmos.* **2011**, *116*, D23113. [CrossRef]
24. Zou, C.Z.; Wang, W.; NOAA CDR Program. *NOAA Fundamental Climate Data Record (FCDR) of AMSU-A Level 1c Brightness Temperature*, Version 1.0.; NOAA National Climatic Data Center: Silver Spring, MD, USA, 2013. [CrossRef]
25. Twarog, E.M.; Purdy, W.E.; Gaiser, P.W.; Cheung, K.H.; Kelm, B.E. WindSat on-orbit warm load calibration. *IEEE Trans. Geosci. Remote Sens.* **2006**, *44*, 516–529. [CrossRef]
26. Wentz, F.; Gentemann, C.L.; Ashcroft, P.D. On-Orbit Calibration of AMSR-E and the Retrieval of Ocean Products. In Proceedings of the 83rd AMS Annual Meeting, Long Beach, CA, USA, 9–13 February 2003; Paper P5.9. Available online: http://images.remss.com/papers/rssconf/wentz_ams_2003_longbeach_amsre_calibration.pdf (accessed on 1 October 2003).
27. Meissner, T.; Wentz, F. Intercalibration of AMSR-E and WindSat brightness temperature measurements over land scenes. In Proceedings of the 2010 IEEE International Geoscience and Remote Sensing Symposium, Honolulu, HI, USA, 25–30 July 2010; pp. 3218–3219. [CrossRef]
28. Cao, C.; Weinreb, M.; Sullivan, J. Solar contamination effects on the infrared channels of the advanced very high resolution radiometer (AVHRR). *J. Geophys. Res.* **2001**, *106*, 33463–33469. [CrossRef]
29. Walton, C.; Sullivan, J.T.; Rao, C.R.N.; Weinreb, M.P. Corrections for detector nonlinearities and calibration inconsistencies of the infrared channels of the advanced very high-resolution radiometer. *J. Geophys. Res.* **1998**, *103*, 3323–3337. [CrossRef]
30. Weng, F.; Zou, X.; Sun, N.; Yang, H.; Tian, M.; Blackwell, W.J.; Wang, X.; Lin, L.; Anderson, K. Calibration of Suomi national polar-orbiting partnership advanced technology microwave sounder. *J. Geophys. Res.* **2013**, *118*, 11,187–11,200. [CrossRef]
31. Jeffrey, R.; Graumann, A. *NOAA KLM USER'S GUIDE with NOAA-N, N Prime, and MetOp SUPPLEMENTS (1-2530)*; National Oceanic and Atmospheric Administration, National Environmental Satellite, Data, and Information Service, National Climatic Data Center: Asheville, NC, USA, 2014.
32. Weng, F.; Zou, X. Errors from Rayleigh–Jeans approximation in satellite microwave radiometer calibration systems. *Appl. Opt.* **2013**, *52*, 505–508. [CrossRef] [PubMed]
33. Zou, C.; Qian, H. *Prelaunch Calibration of the Advanced Microwave Sounding Unit-A Radiometer for MetOp-C*; NOAA/STAR Technical Report; United States Department of Commerce: Washington, DC, USA, 2018.
34. Bell, S.A. *Beginner's Guide to Uncertainty of Measurement*; National Physical Laboratory: Middlesex, UK, 1999; Issue 2; p. 33.
35. Zou, C.-Z.; Xu, H.; Hao, X.; Fu, Q. Post-millennium atmospheric temperature trends observed from satellites in stable orbits. *Geophys. Res. Lett.* **2021**, *48*, e2021GL093291. [CrossRef]
36. Hans, I.; Burgdorf, M.; John, V.O.; Mittaz, J.; Buehler, S.A. Noise performance of microwave humidity sounders over their life Time. *Atmos. Meas. Tech.* **2017**, *10*, 4927–4945. [CrossRef]
37. Yang, J.X.; Yang, H. A new algorithm for determining the noise equivalent delta temperature of in-orbit microwave radiometers. *IEEE Trans. Geosci. Remote. Sens.* **2021**, *60*, 1–11. [CrossRef]
38. Vallado, D.; Crawford, P.; Hujsak, R.; Kelso, T. Revisiting Spacetrack Report #3. In *Proceedings of the Astrodynamics Specialist Conference, Keystone, CO, USA, 21–24 August 2006*; American Institute of Aeronautics and Astronautics: Reston, VA, USA, 2006; ISBN 978-1-62410-048-2. [CrossRef]
39. Cao, C.; Weinreb, M.; Xu, H. Predicting Simultaneous Nadir Overpasses among Polar-Orbiting Meteorological Satellites for the Intersatellite Calibration of Radiometers. *J. Atmos. Ocean. Technol.* **2004**, *21*, 537–542. [CrossRef]
40. Joint Polar Satellite System (JPSS). *Advanced Technology Microwave Sounder (ATMS) SDR Calibration Algorithm Theoretical Basis Document (ATBD)*; Center for Satellite Applications and Research: College Park, MD, USA, 2013. Available online: https://www.star.nesdis.noaa.gov/jpss/documents/ATBD/D0001-M01-S01-001_JPSS_ATBD_ATMS-SDR_B.pdf (accessed on 30 December 2022).